

**Examination of aerosol impacts on convective clouds and precipitation in two metropolitan areas in East Asia; how varying depths of convective clouds between the areas diversify those aerosol effects?**

Seoung Soo Lee<sup>1,2</sup>, Jinho Choi<sup>3</sup>, Goun Kim<sup>4</sup>, Kyung-Ja Ha<sup>2,5,6</sup>, Kyong-Hwan Seo<sup>3</sup>, Chang-Hoon Jung<sup>7</sup>, Junshik Um<sup>3</sup>, Youtong Zheng<sup>8</sup>, Jianping Guo<sup>9</sup>

Deleted: <sup>7</sup>

<sup>1</sup>Earth System Science Interdisciplinary Center, University of Maryland, Maryland

<sup>2</sup>Research Center for Climate Sciences, Pusan National University, Busan, Republic of Korea

<sup>3</sup>Department of Atmospheric Sciences, Division of Earth Environmental System, Pusan National University, Busan, Republic of Korea

<sup>4</sup>Marine Disaster Research Center, Korea Institute of Ocean Science and Technology, Pusan, Republic of Korea

<sup>5</sup>Center for Climate Physics, Institute for Basic Science, Busan, Republic of Korea

<sup>6</sup>BK21 School of Earth and Environmental Systems, Pusan National University, Busan, Republic of Korea

<sup>7</sup>Department of Health Management, Kyungin Women's University, Incheon, Republic of Korea

Formatted: Justified

<sup>8</sup>The Program in Atmospheric and Oceanic Sciences, Princeton University,

Deleted: <sup>7</sup>

and National Oceanic and Atmospheric Administration/Geophysical Fluid Dynamics Laboratory, Princeton, New Jersey, USA

<sup>9</sup>State Key Laboratory of Severe Weather, Chinese Academy of Meteorological Sciences, Beijing, China

Deleted: <sup>1</sup>

28 Corresponding author: Seoung Soo Lee  
29 Office: (303) 497-6615  
30 Fax: (303) 497-5318  
31 E-mail: [cumulss@gmail.com](mailto:cumulss@gmail.com), [slee1247@umd.edu](mailto:slee1247@umd.edu)

32  
33  
34  
35  
36  
37  
38  
39  
40  
41  
42  
43  
44  
45  
46  
47  
48  
49  
50  
51  
52  
53  
54

## Abstract

This study examines the role played by aerosols which act as cloud condensation nuclei (CCN) in the development of clouds and precipitation in two metropolitan areas in East Asia that have experienced substantial increases in aerosol concentrations over the last decades. These two areas are the Seoul and Beijing areas and the examination has been done by performing simulations using the Advanced Research Weather Research and Forecasting model as a cloud-system resolving model. CCN are advected from the continent to the Seoul area and this increases aerosol concentrations in the Seoul area. These increased CCN concentrations induce the enhancement of condensation that in turn induces the enhancement of deposition and precipitation amount in a system of less deep convective clouds as compared to those in the Beijing area. In a system of deeper clouds in the Beijing area, increasing CCN concentrations also enhance condensation but reduce deposition. This leads to CCN-induced negligible changes in precipitation amount. Also, in the system, there is a competition for convective energy among clouds with different condensation and updrafts. This competition results in different responses to increasing CCN concentrations among different types of precipitation, which are light, medium and heavy precipitation in the Beijing area. CCN-induced changes in freezing play a negligible role in CCN-precipitation interactions as compared to the role played by CCN-induced changes in condensation and deposition in both of the areas.

Deleted: aerosols

Deleted: as

Deleted: (CSRM)

Deleted: Aerosols

Deleted: aerosol

Deleted: aerosol

Deleted: also

Deleted: aerosol

Deleted: aerosol

Deleted: In both of the areas,

Deleted: aerosol

Deleted: aerosol

Deleted: aerosol

Deleted: and deposition

Deleted: ¶

## 1. Introduction

With increasing aerosol loading or concentrations, cloud-particle sizes can be changed. In general, with increasing droplet sizes, the efficiency of collision and collection among droplets increases. Increasing aerosol loading is known to make the droplet size smaller and thus make the efficiency of collision and collection among droplets lower. This leads to less droplets or cloud liquid forming raindrops and there is more cloud liquid present in the air to be evaporated or frozen. Studies have shown that increases in cloud-liquid mass due to increasing aerosol loading can enhance the freezing of cloud liquid and parcel buoyancy, which lead to the invigoration of convection (Rosenfeld et al., 2008; Fan et al., 2009). Via the invigoration of convection, precipitation can be enhanced. The dependence of aerosol-induced invigoration of convection and precipitation enhancement on aerosol-induced increases in condensational heating in the warm sector of a cloud system has been shown (e.g., van den Heever et al., 2006; Fan et al., 2009; Lee et al., 2018). Increasing cloud-liquid mass induces increasing evaporation, which intensifies gust fronts. This in turn strengthens convective clouds and increases the amount of precipitation (Khain et al., 2005; Tao et al., 2007; Storer et al., 2010; Tao et al., 2012; Lee et al., 2017; Lee et al., 2018). It is notable that aerosol-induced precipitation enhancement is strongly sensitive to cloud types that can be defined by cloud characteristics such as cloud depth (e.g., Tao et al., 2007; Lee et al., 2008; Fan et al., 2009).

Since East Asia was industrialized, there have been substantial increases in aerosol concentrations over the last decades in East Asia (e.g., Lee et al., 2013; Lu et al., 2011; Oh et al., 2015; Dong et al., 2019). These increases are far greater than those in other regions such as North America and Europe (e.g., Lu et al., 2011; Dong et al., 2019). While those increasing aerosols affect clouds, precipitation and hydrologic circulations in the continental East Asia, the increase in the advected aerosols from the continent to the Korean Peninsula affect clouds, precipitation and hydrologic circulations in the Korean Peninsula (Kar et al., 2009). This study aims to examine effects of the increasing aerosols, which particularly act as cloud condensation nuclei (CCN), and their advection on clouds and precipitation in East Asia. This study focuses on aerosols which act as CCN, but not ice-nucleating particles (INPs), to examine those effects, based on the fact that CCN

**Deleted:** and autoconversion, which represent cloud microphysical properties, ...

**Deleted:** Autoconversion is a process where cloud-liquid particles or droplets grow to form raindrops via collision and collection among droplets.

**Deleted:** particle

**Deleted:** particle

**Deleted:** ,

**Deleted:** and autoconversion

**Deleted:** which can grow to be

**Deleted:** ¶



account for most of aerosol mass that affects clouds and precipitation, and CCN, but not INPs, are associated with above-described aerosol-induced invigoration of convection and intensification of gust fronts. Note that these aerosol-induced invigoration and intensification are two well-established major theories of aerosol-cloud interactions. As a first step to the examination, this study focuses on two metropolitan areas in East Asia which are the Beijing and Seoul areas. The population of each of the Beijing and Seoul areas is ~ 20 millions. Associated with this, these areas have lots of aerosol sources (e.g., traffic) and have made a substantial contribution to the increases in aerosol concentrations in East Asia. Hence, we believe that these two cities can represent overall situations related to increasing aerosol concentrations in East Asia.

As mentioned above, aerosol-cloud interactions (and their impacts on precipitation) are strongly dependent on cloud types and thus to gain a more general understanding of those interactions, we select cases from the Beijing and Seoul areas with different cloud types. A selected case from the Beijing area involves deep convective clouds that reach the tropopause, while a selected case from the Seoul area involves comparatively shallow (or less deep) convective clouds. Via comparisons between these two cases, we aim to identify mechanisms that control varying aerosol-cloud interactions with cloud types.

To examine impacts of aerosols, which act as CCN, on clouds and precipitation in the cases, numerical simulations are performed, as a way of fulfilling above-described aim. These simulations use a cloud-system resolving model (CSRM) that has reasonably high resolutions to resolve cloud-scale processes that are related to cloud microphysics and dynamics. Hence, these simulations are able to find process-level mechanisms in association with cloud-scale processes.

## 2. Case description

In the Seoul area, South Korea, there is an observed mesoscale convective system (MCS) for a period from 03:00 LST (local solar time) to 18:00 LST December 24<sup>th</sup> 2017. During this period, there is a recorded moderate amount of precipitation and its maximum precipitation rate reaches ~ 13 mm hr<sup>-1</sup>. Here, precipitation in the Seoul area is measured by rain gauges in automatic weather stations (AWSs) (King, 2009). The measurement is

Deleted: is

performed hourly with a spatial resolution that ranges from ~1 km to ~10 km. The Seoul area is marked by an inner rectangle in Figure 1a and Figure 2a and dots in the rectangle in Figure 2a mark the selected locations of rain gauges. At 21:00 LST December 23<sup>rd</sup> 2017, synoptic-scale features develop in favor of the formation and development of the selected MCS and associated moderate rainfall. A low-pressure trough was over northeast China and the Yellow Sea (Figure 1a). Along the flank of the low-pressure system, there was the southwesterly low-level jets to transport warm and moist air. This warm and moist air is originated from the Yellow Sea and transported to the Korean Peninsula (Figure 1a). The southwesterly low-level jet plays an important role in the formation and development of rainfall events in the Korean Peninsula by fetching warm and moist air (Hwang and Lee 1993; Lee et al. 1998; Seo et al. 2013; Oh et al. 2018).

There was another observed MCS case in the Beijing area, China for a period from 14:00 LST on July 27<sup>th</sup> to 00:00 LST July 28<sup>th</sup> 2015. There is a substantial recorded amount of precipitation for this period and its maximum precipitation rate reaches ~ 45 mm hr<sup>-1</sup>. Here, similar to the situation in the Seoul area, precipitation in the Beijing area is measured by rain gauges in AWSs hourly with a spatial resolution that ranges from ~1 km to ~10 km. The Beijing area is marked by an inner rectangle in Figure 1b and Figure 2b and dots in the rectangle in Figure 2b mark the selected locations of rain gauges. At 09:00 LST July 27<sup>th</sup> 2015, synoptic-scale features develop in favor of the formation and development of the selected MCS. The southerly low-level jet forms and develops heavy rainfall events in the Beijing area by transporting warm and moist air to the area (Figure 1b). Note that synoptic features in Figures 1a and 1b are based on reanalysis data that are produced by the Met Office Unified Model (Brown et al., 2012) every 6 hours with a  $0.11^\circ \times 0.11^\circ$  resolution.

### 3. CSRM and simulations

#### 3.1 CSRM

The Advanced Research Weather Research and Forecasting (ARW) model (version 3.3.1) is used as a CSRM. The ARW model is a compressible model with a nonhydrostatic status.

Deleted:

Formatted: Body Text 3, Left, Level 2

Moved (insertion) [1]

Deleted: The automatic weather system (AWS) operates at the surface and rain gauges in the AWS measure precipitation hourly with a spatial resolution of ~1 km.

A 5th-order monotonic advection scheme is used to advect microphysical variables (Wang et al., 2009). The Rapid Radiation Transfer Model (RRTMG; Mlawer et al., 1997; Fouquart and Bonnel, 1980) is adopted to parameterize shortwave and longwave radiation in simulations. A microphysics scheme that is used in this study calculates the effective sizes of hydrometeors that are fed into the RRTMG, and the RRTMG simulates how these effective sizes affect radiation.

The CSRM adopts a bin scheme as a way of parameterizing microphysics. The Hebrew University Cloud Model (HUCM) detailed in Khain et al. (2011) is the bin scheme. A set of kinetic equations is solved by the bin scheme to represent size distribution functions for each class of hydrometeors and aerosols acting as CCN. The hydrometeor classes are water drops, ice crystals (plate, columnar and branch types), snow aggregates, graupel and hail. Drops whose radius is smaller (larger) than 40  $\mu\text{m}$  are categorized to be droplets (raindrops). There are 33 bins for each size distribution in a way that the mass of a particle  $m_j$  in the  $j$  bin is to be  $m_j = 2m_{j-1}$ .

A cloud-droplet nucleation parameterization based on Köhler theory represents cloud-droplet nucleation. Arbitrary aerosol mixing states and aerosol size distributions can be fed to this parameterization. To represent heterogeneous ice-crystal nucleation, parameterizations by Lohmann and Diehl (2006) and Möhler et al. (2006) are used. In these parameterizations, contact, immersion, condensation-freezing, and deposition nucleation paths are all considered by taking into account the size distribution of INPs, temperature and supersaturation. Homogeneous droplet freezing is considered following the theory developed by Koop et al. (2000).

Deleted: cloud condensation nuclei (

Deleted: )

Deleted: ¶

### 3.2 Control runs

For a three-dimensional CSRM simulation of the observed case of convective clouds in the Seoul (Beijing) area, i.e., the control-s (control-b) run, a domain just over the Seoul (Beijing) area, which is shown in Figure 1a (1b) and Figure 2a (2b), is used. This domain adopts a 300-m resolution. The control-s run is for a period from 03:00 LST to 18:00 LST December 24<sup>th</sup> 2017, while the control-b run is for a period from 14:00 LST on July 27<sup>th</sup> to 00:00 LST July 28<sup>th</sup> 2015. The length of the domain is 170 (140) km in the east-west

(north-south) direction for the control-s run, and 280 (240) km for the control-b run. There are 100 vertical layers and these layers employ a sigma coordinate that follows the terrain. The top pressure of the model is 50 hPa for both of the control-s and control-b runs. On average, the vertical resolution is ~200 m.

Reanalysis data, which are produced by the Met Office Unified Model, represent the synoptic-scale features, provide initial and boundary conditions of variables such as wind, potential temperature, and specific humidity for the simulations. The simulations adopt an open lateral boundary condition. The Noah land surface model (LSM; Chen and Dudhia, 2001) calculates surface heat fluxes.

The current version of the ARW model is not able to consider the spatiotemporal variation of aerosol properties. In order to take into account the spatiotemporal variation of aerosol properties, which is typical in metropolitan areas, such as composition and number concentration, an aerosol preprocessor, which is able to consider the variability of aerosol properties, is developed and used in the simulations. This aerosol preprocessor interpolates or extrapolates background aerosol properties in observation data such as aerosol mass (e.g., PM<sub>2.5</sub> and PM<sub>10</sub>) into grid points and time steps in the model. In this study, the inverse distance weighting method is used for the extrapolation and interpolation of observation data including aerosol mass into grid points and time steps in the model. PM stands for particulate matter. The mass of aerosols with diameter smaller than 2.5 (10.0) µm per unit volume of the air is PM<sub>2.5</sub> (PM<sub>10</sub>).

PM<sub>2.5</sub> or PM<sub>10</sub>, which are measured by surface observation sites in the domains, is used to consider the variability of aerosol properties. The distance between the observation sites ranges from ~1 km to ~10 km and the time interval between observations of aerosol mass is ~10 minutes; the selected locations of these sites are marked by dots in the inner rectangles in Figure 2. Hence, the variability is represented by fine spatiotemporal resolutions of the sites. The ground sites that are equipped with the aerosol robotic network (AERONET; Holben et al., 2001) are in the domains. Distances between these sites are ~10 km. In this study, PM<sub>2.5</sub>/PM<sub>10</sub> data are used to represent the spatiotemporal variability of aerosols over the domains and the simulation periods. To represent aerosol composition and size distributions, data from the AERONET sites are employed.

Deleted:

Deleted: The Met Office Unified Model (Brown et al., 2012) produces these data every 6 hours with a  $0.11^\circ \times 0.11^\circ$  resolution.

Moved down [2]: Here, it is assumed that the mass of aerosols that act as CCN is represented by PM<sub>2.5</sub> and PM<sub>10</sub> for the Seoul and Beijing areas, respectively.

Deleted: is

Deleted:

Deleted: .

Deleted: acting as CCN

The AERONET data are averaged over the AERONET sites at 02:00 LST December 24<sup>th</sup> 2017 (13:00 LST July 27<sup>th</sup> 2015), which is 1 hour before the observed MCS forms, for the Seoul (Beijing) case. Based on the average data, it is assumed that aerosol particles are internally mixed with 70 (80) % ammonium sulfate and 30 (20) % organic compound for the Seoul (Beijing) case. This mixture is assumed to represent aerosol chemical composition in the whole domain and during the entire simulation period. Since ammonium sulfate and organic compound are representative components of CCN, it is assumed that the mass of aerosols that act as CCN is represented by PM<sub>2.5</sub> and PM<sub>10</sub> for the Seoul and Beijing areas, respectively. Aerosols reflect, scatter and absorb shortwave and longwave radiation before they are activated. This type of aerosol-radiation interactions is not taken into account in this study. This is mainly based on the fact that in the mixture, there is insignificant amount of radiation absorbers; black carbon is a representative radiation absorber. The AERONET observation indicates that the size distribution of background aerosols acting as CCN follows the tri-modal log-normal distribution for the Seoul (Beijing) case as exemplified in Figure 3a (3b). It is assumed that for the whole domain and simulation period, the size distribution of background aerosols acting as CCN follows the shape of distribution with specific size distribution parameters (i.e., modal radius and standard deviation of each of Aitken, accumulation and coarse modes, and the partition of aerosol number among those modes) as shown in Figure 3a (3b) for the Seoul (Beijing) case. Modal radius of the shape of distribution is 0.015 (0.012), 0.110 (0.085), and 1.413 (1.523)  $\mu\text{m}$ , while standard deviation of the shape of distribution is 1.28 (1.10), 1.54 (1.63), and 1.75 (1.73) for Aitken, accumulation and coarse modes, respectively, in the Seoul (Beijing) case. The partition of aerosol number, which is normalized by the total aerosol number of the size distribution, is 0.555 (0.612), 0.444 (0.387), and 0.001 (0.001) for Aitken, accumulation and coarse modes, respectively, in the Seoul (Beijing) case. The distribution parameters of the assumed shape of the size distribution of background aerosols in Figure 3a (3b) are those that are averaged over the AERONET sites at a time point, which is 1 hour before the observed MCS form, for the Seoul (Beijing) case. By using PM<sub>2.5</sub> or PM<sub>10</sub>, which is interpolated and extrapolated to grid points immediately above the surface and time steps, and based on the assumption of aerosol composition and size distribution above, the background number concentrations of aerosols acting as CCN

Deleted: For the period with the observed clouds

Deleted: , based on t

Formatted: Superscript

Formatted: Superscript

Deleted: ,

Deleted: on average,

Moved (insertion) [2]

Deleted: Here,

Deleted: , based on the fact that aerosol composition does not vary significantly over the domain and during the whole period with the observed clouds.

Deleted: s

Deleted: Hence, it

Deleted: nuclei

Deleted: T

Deleted: is

Deleted: with

Deleted: the average of the distribution parameters

Deleted: and the period with

Deleted: clouds

Deleted: Since the AERONET observation shows that the shape of the size distribution does not vary significantly over the domain and during the simulation period for each of the Seoul and Beijing cases, we believe that the assumption is reasonable.

Deleted: and

Deleted:

are obtained ~~for the simulation for each of the cases.~~ There is no variation with height in background ~~concentrations of aerosols acting as CCN~~ from immediately above the surface to the top of the planetary boundary layer (PBL). However, it is assumed that they decrease exponentially with height from the PBL top upward. ~~With this exponential decrease, when the altitude reaches the tropopause, background concentrations of aerosols acting as CCN reduce by a factor of ~10 as compared to those at the PBL top. The size distribution and composition of aerosols acting as CCN~~ do not vary with height. Once background aerosol properties (i.e., aerosol number concentrations, size distribution and composition) are put into each grid point and time step, those properties at each grid point and time step do not change during the course of the simulations.

For the control-s and control-b runs, aerosol properties of ~~INPs~~ are not different from those of CCN except for the fact that the concentration of background aerosols acting as CCN is 100 times higher than the concentration of background aerosols acting as ~~INPs~~ at each time step and grid point, following a general difference between CCN and ~~INPs~~ in terms of their concentrations (Pruppacher and Klett, 1978).

Once clouds form and background aerosols start to be in clouds, those aerosols are not background aerosols anymore and the size distribution and concentrations of those aerosols begin to evolve through aerosol sinks and sources that include advection and aerosol activation (Fan et al., 2009). For example, once aerosols are activated, they are removed from the corresponding bins of the aerosol spectra. In clouds, after aerosol activation, aerosol mass starts to be inside hydrometeors and via collision-collection, it transfers to different types and sizes of hydrometeors. In the end, aerosol mass disappears in the atmosphere when hydrometeors with aerosol mass touches the surface. In non-cloudy areas, aerosol size and spatial distributions are designed to be identical to the size and spatial distributions of background aerosols, respectively. In other words, for this study, we use “the aerosol recovery method”. In this method, at any grid points, immediately after clouds disappear entirely, aerosol size distributions and number concentrations recover to background properties that background aerosols at those points have before those points are included in clouds. In this way, we can keep ~~concentrations of background aerosols~~ outside clouds in the simulations at observed counterparts. ~~This enables spatiotemporal distributions of background aerosols in the simulations to mimic those distributions that~~

**Deleted:** These background number concentrations, associated aerosol size distribution and composition are interpolated or extrapolated to grid points immediately above the surface and time steps in the simulation for each of the cases.

**Deleted:** aerosol

**Deleted:** Aerosol

**Deleted:** s

**Formatted:** Font: (Asian) Times New Roman

**Deleted:** ice-nucleating particles (

**Deleted:** )

**Deleted:** aerosol c

**Deleted:** Thus, we are able to simulate

**Deleted:** aerosol evolutions,

**Deleted:** via processes such as transportation of background aerosols by wind (or aerosol advection)

**Deleted:** ,

are observed and particularly associated with observed aerosol advection in reality. In the aerosol recovery method, there is no time interval between the cloud disappearance and the aerosol recovery. Here, when the sum of mass of all types of hydrometeors (i.e., water drops, ice crystals, snow aggregates, graupel and hail) is not zero at a grid point, that grid point is considered to be in clouds. When this sum becomes zero, clouds are considered to disappear. Many studies using CSRM have employed this aerosol recovery method. They have proven that with the recovery method, reasonable simulations of overall cloud and precipitation properties are accomplished (e.g., Morrison and Grabowski, 2011; Lebo and Morrison, 2014; Lee et al., 2016; Lee et al., 2018).

### 3.3 Additional runs

We repeat the control-s run by getting rid of aerosol-advection induced increases in concentrations of aerosols acting as CCN as a way of investigating how the aerosol advection affects the cloud system in the Seoul area. This repeated run is named the low-aerosol-s run. An aerosol layer, which is advected from East Asia or from the west of the Seoul area to it, increases aerosol concentrations in the Seoul area. There are stations in islands in the Yellow Sea that monitor the aerosol advection (Eun et al., 2016; Ha et al., 2019). To monitor and identify the aerosol advection,  $PM_{2.5}$  which is measured by a station in Baekryongdo island in Yellow Sea are compared to those which are measured in stations in and around the Seoul area. In Figure 2a, a dot outside the inner rectangle marks the island. The time evolution of  $PM_{2.5}$  measured by the station on the island and the average  $PM_{2.5}$  over stations in the Seoul area, between 07:00 LST on December 22<sup>nd</sup> and 21:00 LST on December 24<sup>th</sup> in 2017 when there is the strong advection of aerosols from East Asia to the Seoul area, is shown in Figure 4. At 09:00 LST on December 22<sup>nd</sup>, the advection of aerosols from East Asia enables aerosol mass to start going up and attain its peak around 05:00 LST on December 23<sup>rd</sup> on the island. Following this, aerosol mass starts to increase in the Seoul area around 01:00 LST on December 23<sup>rd</sup>, and the mass attains its peak at 15:00 LST on December 23<sup>rd</sup> in the Seoul area. This is because aerosols, which are advected from East Asia, move through the island to reach the Seoul area.

Deleted: as

Deleted: observed

Deleted: ,

Deleted: in case we neglect possible errors from the assumption on aerosol size distribution and composition, and the process where observed data are interpolated or extrapolated to grid points and time steps in the simulations.

Deleted: aerosol

Deleted: and

Deleted: a

Deleted: and the Seoul area, respectively

Deleted:

In the low-aerosol-s run, as a way of getting rid of aerosol-advection induced increases in concentrations of aerosols acting as CCN, it is assumed that  $PM_{2.5}$ , which is assumed to represent the mass of aerosols acting as CCN, and the associated background concentration of aerosols acting as CCN after 01:00 LST on December 23<sup>rd</sup> do not evolve with the aerosol advection in the Seoul area. Hence, the background concentration of aerosols acting as CCN is assumed to have that at 01:00 LST on December 23<sup>rd</sup> at each time step and grid point at the beginning of the simulation period. However, to isolate CCN effects on clouds, background aerosol concentration acting as INPs at each time step and grid point in the low-aerosol-s run is not different from that in the control-s run during the simulation period. In the observed PM data for the Seoul area, there is reduction in PM by a factor of  $\sim 10$  on average over a period between  $\sim 07:00$  and  $\sim 14:00$  LST on December 24<sup>th</sup>, since precipitation scavenges aerosols (Figure 4). To emulate this scavenging and reflect it in background aerosols acting as CCN for the low-aerosol-s run,  $PM_{2.5}$  and corresponding background concentrations of aerosols acting as CCN at each grid point is gradually reduced for the period between 07:00 and 14:00 LST on December 24<sup>th</sup>. This reduction is done in a way that background concentrations of aerosols acting as CCN at each grid point at 14:00 LST on December 24<sup>th</sup> is 10 times lower than that at 07:00 LST on December 24<sup>th</sup> in the low-aerosol-s run. Then,  $PM_{2.5}$  and corresponding background concentrations of aerosols acting as CCN at each grid point at 14:00 LST on December 24<sup>th</sup> maintains until the end of the simulation period. This results in the evolution of the average  $PM_{2.5}$  over the Seoul area in the low-aerosol-s run as shown in Figure 4. Here, the concentration of background aerosols acting as CCN, which is averaged over the whole domain and simulation period, in the control-s run is 3.1 times higher than that in the low-aerosol-s run. Via comparisons between the runs, how the increasing concentration of background aerosols acting as CCN due to the aerosol advection has an impact on clouds can be examined. The concentration of background aerosols acting as CCN is different among grid points and time steps in the control-s run. Hence, the ratio of the concentration of background aerosols acting as CCN between the runs is different among grid points and time steps.

For the Beijing case, to examine how aerosols acting as CCN affect clouds and precipitation, we repeat the control-b run with simply reduced concentrations of

Deleted: the

Deleted:

Deleted: concentrations

Formatted: Subscript

Deleted: thus

Deleted: aerosol

Deleted: s

Formatted: Subscript

Deleted: aerosol

Deleted: s

Deleted: aerosol

Formatted: Subscript

Deleted: aerosol

Formatted: Subscript

Deleted: ird



background aerosols acting as CCN at each time step and grid point by a factor of 3.1. This repeated run is named the low-aerosol-b run. The 3.1-fold increase in aerosol concentrations from the low-aerosol-b run to the control-b is based on the 3.1-fold increase in the average concentration of background aerosols acting as CCN from the low-aerosol-s run to the control-s run. However, as in the control-s and low-aerosol-s runs, to isolate CCN effects on clouds, background aerosol concentration acting as INPs at each time step and grid point in the low-aerosol-b run is identical to that in the control-b run during the simulation period. Hence, on average, a pair of the control-s and low-aerosol-s runs has the same perturbation of aerosols acting as CCN as in a pair of the control-b and low-aerosol-b runs. Here, we define aerosol perturbation as a relative increase in aerosol concentration when compared to that before the increase occurs. The brief summary of all simulations in this study is given in Table 1.

## 4. Results

### 4.1 Cumulative precipitation

We compare the observed precipitation to the simulated counterpart in the control-s run for the Seoul case and in the control-b run for the Beijing case. For this comparison, the observed and simulated precipitation rates at the surface are averaged over the domain for each of the Seoul and Beijing cases (Figures 5a and 5b). Here, the simulated precipitation rates are smoothed over 1 hour. The comparison shows that the evolution of the simulated precipitation rate does not deviate from the observed counterpart significantly (Figures 5a and 5b).

In the Seoul case, overall, the precipitation rate is higher in the control-s run than in the low-aerosol-s run. As a result of this, the domain-averaged cumulative precipitation amount at the last time step is 14.1 mm and 12.0 mm in the control-s run and the low-aerosol-s run, respectively. The control-s run shows ~20 % higher cumulative precipitation amount. In the Beijing case, the evolution of the mean precipitation rate in the control-b run is not significantly different from that in the low-aerosol-b run. Due to this, the control-b run shows only ~2 % higher cumulative precipitation amount, despite the fact that the

Deleted: aerosol

Moved up [1]: The automatic weather system (AWS) operates at the surface and rain gauges in the AWS measure precipitation hourly with a spatial resolution of ~1 km.

concentrations of background aerosols acting as CCN are ~3 times higher in the control-b run than in the low-aerosol-b run. Note that in the Seoul case, the time- and domain-averaged concentration of background aerosols acting as CCN is also ~3 times higher in the control-s run than in the low-aerosol-s run. Despite this, the difference in the cumulative precipitation amount between the runs with different concentrations of background aerosols acting as CCN is greater in the Seoul case than in the Beijing case.

## 4.2 Precipitation, and associated latent-heat and dynamic processes

Figures 6a and 6b show the cumulative frequency distributions of precipitation rates at the last time step in the simulations for the Seoul and Beijing cases, respectively. In each of those figures, the observed frequency distribution is shown and compared to the simulated distribution. The observed distribution is obtained by interpolating and extrapolating the observed precipitation rates to grid points and time steps in each of the control-s and control-b runs. The observed maximum precipitation rates are 13.0 and 44.5 mm hr<sup>-1</sup> for the Seoul and Beijing cases, respectively, and these maximum rates are similar to those in the control-s and control-b runs, respectively. Overall, the observed and simulated frequency distributions are in good agreement for each of the cases. This enables us to assume that results in the control-s (control-b) run are benchmark results to which results in the low-aerosol-s (low-aerosol-b) run can be compared to identify how aerosols acting as CCN have an impact on clouds and precipitation for the Seoul (Beijing) case. Here, it is notable that for the Beijing case, while differences in the cumulative precipitation amount between the control-b and low-aerosol-b runs are not significant, features in the frequency distribution of precipitation rates between those runs are substantially different (Figure 6b).

### 1) Seoul case

#### a. Precipitation Frequency distributions

Regarding precipitation whose rates are higher than ~2 mm hr<sup>-1</sup>, the cumulative precipitation frequency at the last time step is higher in the control-s run as compared to

Deleted:

that in the low-aerosol-s run (Figure 6a). In particular, for the precipitation rate of 11.4 mm hr<sup>-1</sup>, there is an increase in the cumulative frequency by a factor of as much as ~10 in the control-s run. When it comes to precipitation rates above 11.5 mm hr<sup>-1</sup>, precipitation is present in the control-s run and precipitation is absent in the low-aerosol-s run. Regarding precipitation whose rates are lower than ~2 mm hr<sup>-1</sup>, differences in the cumulative frequency between the runs are insignificant. Hence, we see that there are significant increases in the frequency of relatively heavy precipitation whose rates are above ~2 mm hr<sup>-1</sup> in the control-s run when compared to that in the low-aerosol-s run. At the last time step, this results in a larger amount of cumulative precipitation in the control-s run than in the low-aerosol-s run.

The time evolution of the cumulative precipitation frequency is shown in Figure 7. At 06:00 LST December 24<sup>th</sup> 2017, which corresponds to the initial stage of the precipitation development, the maximum precipitation rate reaches ~3 mm hr<sup>-1</sup> and there is the greater frequency over most of precipitation rates in the control-s run than in the low-aerosol-s run (Figure 7a). With the time progress from 06:00 LST to 10:00 LST, the maximum precipitation rate increases to reach 12 mm hr<sup>-1</sup> and the cumulative frequency is higher over precipitation whose rates are higher than ~3 mm hr<sup>-1</sup> in the control-s run, while for precipitation whose rates are lower than ~3 mm hr<sup>-1</sup>, differences in the cumulative frequency between the runs are negligible (Figures 7a and 7b). When time reaches 12:00 LST, which is around time when the peak in the evolution of the area-averaged precipitation rates occurs and thus the system is at its mature stage, the maximum precipitation rate increases up to ~13 mm hr<sup>-1</sup> (Figures 5a and 7c). The basic patterns of differences in the cumulative precipitation frequency between the runs with the maximum precipitation rate around 13 mm hr<sup>-1</sup>, which are established at 12:00 LST, maintain until the end of the simulation period (Figures 6a and 7c).

#### b. Condensation, deposition, updrafts and associated variables

Note that the source of precipitation is precipitable hydrometeors which are raindrops, snow, graupel and hail particles. Droplets and ice crystals are the source of those precipitable hydrometeors mostly via collision and coalescence processes. Droplets and ice

Deleted: T

Deleted: are

Deleted: s

Deleted: when it comes to specific ranges of precipitation whose rates are higher than ~2 mm hr<sup>-1</sup>

Deleted: ~

Deleted:

Deleted: , 7b, 7c and

Deleted: d

Deleted: a

Deleted: .

Deleted: e

Deleted: among droplets and ice crystals

crystals gain their mass mostly via condensation and deposition. Based on this, to explain the greater cumulative precipitation amount in the control-s run than in the low-aerosol-s run, the evolutions of differences in condensation, deposition and associated updrafts between the runs are analyzed. The vertical profiles of differences in the area-averaged condensation, deposition and freezing rates, updraft mass fluxes and the associated mass density of each class of hydrometeors between the runs at 03:20, 03:40, 06:00 and 12:00 LST are shown in Figure 8. In Figure 8, differences in freezing rates are added for a more comprehensive understanding of processes that are related to differences in cumulative precipitation amount between the runs. Freezing includes riming processes between liquid and solid hydrometeors and these riming processes act as a source of precipitable hydrometeors. Cloud fractions are 0.32 (0.30), 0.85 (0.82), 0.93 (0.92) and 1.00 (1.00) in the control-s (low-aerosol-s) run at 03:20, 03:40, 06:00 and 12:00 LST, respectively. We see that cloud fraction does not vary significantly between the runs. Note that in all of figures, which display snow and hail mass density and include Figure 8, snow mass density includes ice-crystal mass density, while hail mass density includes graupel mass density for the sake of the display brevity. In Figure 8, horizontal black lines represent the altitudes of freezing and melting.

Condensation rates in the control-s run start to be larger than that in the low-aerosol-s run at 03:20 LST (Figure 8a). Higher aerosol or CCN concentrations induce more nucleation of droplets, higher cloud droplet number concentration (CDNC) and associated greater integrated surface of droplets in the control-s run. CDNC, which is averaged over grid points and time steps with non-zero CDNC, is 1050 and 352  $\text{cm}^{-3}$  in the control-s and low-aerosol-s runs, respectively. Hence, more droplet surface is provided for water vapor to condense onto in the control-s run. This leads to more condensation in the control-s run. This establishes stronger feedbacks between updrafts and condensation, leading to greater droplet (or cloud-liquid) mass at 03:20 LST in the control-s run (Figure 8a). Then, these stronger feedbacks, which involve stronger updrafts particularly above 2 km in altitude, subsequently induce greater deposition and snow mass as time progresses from 03:20 LST to 03:40 LST, while more condensation and greater droplet mass maintain in the control-s run with the time progress to 03:40 LST (Figure 8b). These stronger updrafts enable clouds to grow higher in the control-s run. This eventually leads to a situation where the maximum

Deleted: and

Deleted: , respectively

Deleted: .

Deleted:

Deleted:

Deleted:

Deleted: and

Deleted: variables

Formatted: Font: (Default) Times New Roman, (Asian) Malgun Gothic, 12 pt, Font color: Auto

Formatted: Font: (Default) Times New Roman, (Asian) Malgun Gothic, 12 pt, Font color: Auto

Formatted: Font: (Default) Times New Roman, (Asian) Malgun Gothic, 12 pt, Font color: Auto

Formatted: Font: (Default) Times New Roman, (Asian) Malgun Gothic, 12 pt, Font color: Auto

Deleted: throughout all altitudes

Formatted: Superscript

Deleted: induces

Deleted: more water vapor to be condensed to

Deleted: mass

Deleted:

Deleted: t 03:40 LST in the control-s run

cloud depth is  $\sim 7$  km in the control-s run and this depth is  $\sim 5$  % deeper than that in the low-aerosol-s run for the whole simulation period.

Through aerosol-induced stronger feedbacks between condensation, deposition and updrafts in the control-s run, while more condensation and more overall deposition maintain in the control-s run, differences in condensation and deposition between the control-s and low-aerosol-s runs increase as time progresses from 03:40 LST to 06:00 LST (Figures 8b and 8c). Associated with this, the greater mass of raindrops and hail particles appears up, while the greater mass of droplets and snow in the control-s run than in the low-aerosol-s run maintains with the time progress from 03:40 LST to 06:00 LST (Figure 8c). At 06:00 LST, there is more freezing starting to occur in the control-s run than in the low-aerosol-s run. However, differences in freezing are  $\sim$ one and  $\sim$ two orders of magnitude smaller than those in deposition and condensation, respectively. After 06:00 LST until time reaches 12:00 LST when the overall differences in the cumulative precipitation frequency between the runs are established, differences in freezing become at an order of magnitude, which is similar to that of differences in deposition, and become around one order of magnitude smaller than those in condensation (Figures 8c and 8d). The greater mass of hydrometeors in the control-s run also continues after 06:00 LST until time reaches 12:00 LST (Figures 8c and 8d). At 12:00 LST, condensation, deposition and freezing rates are still higher in the control-s run. Here, we see that CCN-induced more cumulative precipitation amount and associated differences in the precipitation frequency distribution between the control-s and low-aerosol-s runs are primarily associated with CCN-induced more condensation which induce CCN-induced more deposition and higher mass density of hydrometeors as sources of precipitation but weakly connected to CCN-induced changes in freezing. This is supported by the fact that the time- and domain-averaged differences in freezing rate are  $\sim$ one to  $\sim$ two order of magnitude smaller than those in condensation and deposition rates.

### c. Condensation frequency distributions and horizontal distributions of condensation and precipitation

Deleted:

Deleted: n and

Deleted: more

Deleted: two

Deleted: to

Deleted: three

Deleted: condensation and

Deleted: A similar situation in terms of relative differences between freezing, condensation and deposition continues

Deleted: a

Deleted:

Deleted:

Deleted: It is notable that

Deleted: a

Deleted: the freezing rate becomes lower in the control-s run.

Deleted: ence, h

Deleted: aerosol

Deleted: aerosol

Deleted: aerosol

Deleted: aerosol

Deleted: ¶

Based on the importance of condensation for CCN-induced changes in precipitation, the horizontal distribution of the column-averaged condensation rates over the domain and the cumulative frequency distribution of the column-averaged condensation rates at each time step is obtained. To better visualize the role of condensation in precipitation, the horizontal distribution of the column-averaged condensation rates is superimposed on that of precipitation rates (Figure 9). At 03:40 LST, condensation mainly occurs around the northern part of the domain as marked by a yellow rectangle. The synoptic wind condition in the marked area favors the collision between northward and southward wind and the associated convergence around the surface (Figures 9a and 9b). This convergence induces updrafts and condensation in the marked area. In the marked area, more aerosols acting as CCN induce more and more extensive condensation, which leads to the higher domain-averaged condensation rates in the control-s run than in the low-aerosol-s run (Figures 8b, 9a and 9b). More droplets are formed on more aerosols acting as CCN and more droplets provide more surface areas where condensation occurs and this enables more and more extensive condensation in the control-s run than in the low-aerosol-s run (Figures 8b, 9a and 9b). At 06:20 LST, a precipitating system is advected into the domain via the western boundary, and as seen in Figures 9c and 9d for 07:20 LST, as time progresses to 07:20 LST, the advected precipitating system is further advected to the east and extended mostly over areas in the northern part of the domain where condensation mainly occurs. This confirms that condensation is the main source of cloud mass and precipitation. In the eastern part of the domain, there are mountains and in particular, higher mountains are on the northeastern part of the domain than in the other parts of the domain. These higher mountains induce forced convection and associated condensation more effectively in the northeastern part than in the other parts. This is in favor of the precipitating system that extends further to the east in the northern part of the domain. Due to more aerosols acting as CCN, condensation, which is induced by forced convection over mountains, is more and more extensive in the control-s run (Figures 9c and 9d).

As time progresses to 08:40 LST, the precipitating system moves eastward further in the northern part of the domain and the system in the control-s run extends to the east further as compared to that in the low-aerosol-s run (Figures 9e and 9f). In association with more aerosols acting as CCN and associated more condensation over mountains in the

Deleted: aerosol

Deleted: (Figures 9c and 9d).

Deleted: A

Deleted: ,

Deleted: , 9e and 9f for 06:20 and

Deleted: , respectively,

Deleted: from 06:20 to

Deleted: ,

Deleted: , 9e and 9f

Deleted: 9g, 9h, 9i, 9j,

Deleted: k

Deleted: l

northeastern part, there is more extension of the system in the control-s run than in the low-aerosol-s run. This enables the system in the control-s run to reach the eastern boundary at 08:40 LST, which is earlier than in the low-aerosol-s run (Figures 9e and 9f). The system in the low-aerosol-s run reaches the eastern boundary at 09:00 LST. Here, we see that although aerosols acting as CCN do not change overall locations of the precipitation system, they affect how fast the system extends to the east by affecting the amount of condensation which is produced by forced convection. Associated with this, as seen in Figure 10, the control-s run has the much higher cumulative condensation frequency than the low-aerosol-s run over all of condensation rates during the period between 07:20 and 09:00 LST. Contributed by this, the higher precipitation frequency over most of precipitation rates occurs in the control-s run during and after the period (Supplementary Figures 1a and 1b and Figures 7b and 7c).

At 10:00 LST, in the southern part of the domain, there is a precipitating area forming as marked by a yellow rectangle (Figures 9g and 9h). The precipitation area in the southern part of the domain extends and merge into the advecting main precipitating system in the northern part of the domain as time progresses to 11:00 LST (Figures 9i and 9j). The merge leads to precipitation that occupies most of the domain at 12:00 LST (Figures 9k and 9l). After 10:00 LST, associated with this merge, the maximum precipitation rate increases to 13 mm hr<sup>-1</sup> at 12:00 LST (Figures 7c). After 13:00 LST, the precipitation enters its dissipating stage and its area reduces and nearly disappears. Even after the merge, CCN-induced more condensation maintains and this in turn contributes to a situation where the control-s run has the greater precipitation frequency over most of precipitation rates than in the low-aerosol-s run until the simulations progress to their last time step (Figures 6a, 7c and 8d).

## 2) Beijing case

Stronger convection and deeper clouds develop in the Beijing case than in the Seoul case. The maximum cloud depth is ~7 and ~12 km in the control-s and control-b runs, respectively. In the Seoul case, clouds do not reach the tropopause, while they reach the tropopause in the Beijing case. Deeper clouds in the Beijing case produce the maximum

Deleted: (Figure 9n)

Deleted:

Deleted: Figures 7b and 7c

Deleted: o

Deleted: p

Deleted: during the period between 10:20 and

Deleted: 9q, 9r,

Deleted: s

Deleted: t

Deleted: u

Deleted: v

Deleted: e

Deleted: during the period between 13:00 and 15:20 LST (Figures 9w, 9x, 9y and 9z)

Deleted: aerosol

Deleted: e

Deleted:

Deleted:

precipitation rate of  $\sim 45 \text{ mm hr}^{-1}$  in the control-b run. However, less deep clouds in the Seoul case produce the maximum precipitation rate of  $\sim 13 \text{ mm hr}^{-1}$  in the control-s run (Figure 6).

#### a. Precipitation frequency distributions

When it comes to precipitation whose rates are higher than  $\sim 12 \text{ mm hr}^{-1}$ , the control-b run has the higher cumulative precipitation frequency at the last time step than the low-aerosol-b run (Figure 6b). Particularly, for the precipitation rates of  $28.1$  and  $30.0 \text{ mm hr}^{-1}$ , the cumulative frequency increases by a factor of as much as  $\sim 10$ . Moreover, regarding precipitation rates higher than  $\sim 33 \text{ mm hr}^{-1}$ , precipitation is present in the control-b run, however, precipitation is absent in the low-aerosol-b run. Hence, we see that the frequency of comparatively heavy precipitation whose rates are higher than  $\sim 12 \text{ mm hr}^{-1}$  rises significantly in the control-b run as compared to that in the low-aerosol-b run. Below  $\sim 2 \text{ mm hr}^{-1}$ , there is also the greater precipitation frequency in the control-b run than in the low-aerosol-b run. Unlike the situation for precipitation rates above  $\sim 12 \text{ mm hr}^{-1}$  and below  $\sim 2 \text{ mm hr}^{-1}$ , for precipitation rates from  $\sim 2 \text{ mm hr}^{-1}$  to  $\sim 12 \text{ mm hr}^{-1}$ , the control-aerosol-b run has the lower precipitation frequency than in the low-aerosol-b run. Here, we see that the higher precipitation frequency above  $\sim 12 \text{ mm hr}^{-1}$  and below  $\sim 2 \text{ mm hr}^{-1}$  balances out the lower precipitation frequency between  $\sim 2$  and  $\sim 12 \text{ mm hr}^{-1}$  in the control-b run. This results in the similar cumulative precipitation amount between the runs.

Figure 11 shows the time evolution of the cumulative precipitation frequency. When precipitation starts around 16:00 LST, the higher precipitation frequency occurs over most of precipitation rates in the low-aerosol-run-b run than in the control-b run (Figure 11a). At 16:00 LST, the maximum precipitation rate is lower than  $1.0 \text{ mm hr}^{-1}$  for both of the runs. As time progresses to 17:00 LST, the maximum precipitation rate increases to  $\sim 17 \text{ mm hr}^{-1}$  and the higher (lower) cumulative precipitation frequency over precipitation rates higher than  $\sim 12 \text{ mm hr}^{-1}$  (between  $\sim 2$  and  $\sim 12 \text{ mm hr}^{-1}$ ) in the control-b run than in the low-aerosol-b run, which is described above as shown in Figure 6b for the last time step, starts to emerge (Figure 11b). At 17:20 LST, the higher frequency for precipitation rates below  $2 \text{ mm hr}^{-1}$  in the control-b run, which is also described above as shown in Figure 6b

Deleted: T

Deleted: with respect to some ranges of precipitation rates above  $\sim 12 \text{ mm hr}^{-1}$

Deleted:

Deleted: the

Deleted: ,

Deleted: and the cumulative precipitation frequency starts to be higher (lower) over precipitation rates higher than  $\sim 12 \text{ mm hr}^{-1}$  (between  $\sim 2$  and  $\sim 12 \text{ mm hr}^{-1}$ ) in the control-b run than in the low-aerosol-b run (Figure 11b).

Deleted: the frequency starts to be greater when it comes to

Deleted:



for the last time step, starts to show up, while the higher (lower) frequency for precipitation rates higher than  $\sim 12 \text{ mm hr}^{-1}$  (between  $\sim 2$  and  $\sim 12 \text{ mm hr}^{-1}$ ) in the control-b run, which is established at 17:00 LST, maintains as time progresses from 17:00 LST to 17:20 LST (Figure 11c). At 17:20 LST, the maximum precipitation rate increases to 42 (19)  $\text{mm hr}^{-1}$  in the control-b (low-aerosol-b) run (Figure 11c). At 19:00 LST, the maximum precipitation rate increases to  $\sim 45$  (33)  $\text{mm hr}^{-1}$  for the control-b (low-aerosol-b) run, while the qualitative nature of differences in the precipitation frequency distributions with the tipping precipitation rates of  $\sim 2$  and  $\sim 12 \text{ mm hr}^{-1}$  between the runs does not vary much between 17:20 and 19:00 LST (Figures 11c and 11d). The qualitative nature of differences in the cumulative precipitation frequency between the runs and the maximum precipitation rates in each of the runs, which are established at 19:00 LST, do not vary significantly until the end of the simulation period (Figures 6b and 11d).

#### b. Condensation, deposition, updrafts and associated variables

As done for the Seoul case, as a way of better understanding differences in the cumulative precipitation amount and frequency between the control-b and low-aerosol-b runs, the evolutions of differences in the vertical distributions of the area-averaged condensation rates, deposition rates, freezing rates, the mass density of each class of hydrometeors, and updrafts mass fluxes are obtained and shown in Figures 12. Cloud fractions are 0.12 (0.11), 0.25 (0.22), 0.36 (0.32), 0.43 (0.40) and 0.48 (0.47) in the control-b (low-aerosol-b) run at 14:20, 15:40, 16:00, 17:20 and 19:00 LST, respectively. Here, we see that cloud fraction does not vary significantly between the runs. In Figure 12, horizontal black lines represent the altitudes of freezing and melting. As seen in Figure 5b, precipitation starts around 16:00 LST but differences in condensation rates start at 14:20 LST with higher condensation rates in the control-b run (Figure 12a). Similar to the situation in the Seoul case, higher concentrations of aerosols acting as CCN induce more nucleation of droplets, higher CDNC and associated greater integrated surface of droplets in the control-b run. CDNC, which is averaged over grid points and time steps with non-zero CDNC, is 992 and 341  $\text{cm}^{-3}$  in the control-b and low-aerosol-b runs, respectively. Hence, more droplet surface is provided for water vapor to condense onto in the control-b run. This leads to more

**Deleted:** together with those above  $\sim 12 \text{ mm hr}^{-1}$  in the control-b run, while

**Formatted:** Superscript

**Deleted:**

**Deleted:**

**Deleted:** cloud-liquid and snow mass density

**Formatted:** Font: (Default) Times New Roman, (Asian) Malgun Gothic, 12 pt, Font color: Auto

**Formatted:** Font: (Default) Times New Roman, (Asian) Malgun Gothic, 12 pt, Font color: Auto

**Formatted:** Font: (Default) Times New Roman, (Asian) Malgun Gothic, 12 pt, Font color: Auto

**Formatted:** Font: (Default) Times New Roman, (Asian) Malgun Gothic, 12 pt, Font color: Auto

**Deleted:** aerosol

**Formatted:** Superscript

**Deleted:** induces more water vapor to be condensed to

condensation in the control-b run. Due to this, cloud liquid or droplet mass becomes greater in the control-b run at 14:20 LST (Figure 12a). Increased condensation rates induce increased condensational heating and thus intensified updrafts (Figure 12a). These updrafts enable the maximum cloud depth to be ~ 12 km in the control-b run and this depth is just ~1 % deeper than that in the low-aerosol-b run for the whole simulation period. This negligible difference in the maximum cloud depth between the runs is due to the fact that clouds with the maximum depth reach the tropopause in both of runs and thus there is not much wiggle room to make significant differences in cloud depth between the runs.

When time reaches 15:40 LST, deposition rates and snow mass start to show differences between the runs, while higher condensation rates and droplet mass maintain in the control-b run with the time progress from 14:20 LST to 15:40 LST. However, unlike the situation in the Seoul case, higher concentrations of aerosols acting as CCN result in lower deposition rates and snow mass in the control-b run (Figure 12b). When time progresses from 15:40 LST to 16:00 LST, differences in freezing start to occur and freezing rates are lower (higher) at altitudes between ~6 and ~8 km (~4 and ~6 km), while higher condensation rates and droplet mass, and lower snow mass maintain in the control-b run (Figure 12c). Due to stronger updrafts, which are mainly ascribed to more condensation, deposition rates start to be higher at altitudes between ~7 and ~9 km and freezing rates are higher at altitudes between ~4 and ~6 km in the control-b run with the time progress from 15:40 LST to 16:00 LST (Figure 12c). Differences in freezing rates are at the same order of magnitude of those in deposition and ~two orders of magnitude smaller than those in condensation at 16:00 LST (Figure 12c). At 16:00 LST, differences in hail mass between the runs appear up and hail mass is slightly lower in the control-b run (Figure 12c). At 17:20 LST, overall, freezing rates are lower at altitudes between ~4 and ~8 km, while overall, snow and hail mass is still lower, and droplet mass is still higher in the control-b run (Figure 12d). Differences in freezing rates are at the same order of magnitude of those in deposition and ~one orders of magnitude smaller than those in condensation at 17:20 LST (Figure 12d). Due to more condensation and droplet mass, greater raindrop mass appears up in the control-b run at 17:20 LST (Figure 12d). As the time progresses to 19:00 LST, deposition rates become lower at the altitudes from ~7 km to ~12 km and overall freezing rates become higher at altitudes from ~4 km to ~10 km in the control-b run (Figure

Deleted:

Deleted: as a source of precipitation

Deleted: s

Deleted: h

Deleted: aerosol

Deleted: s

Deleted:

Deleted: reaches

Deleted:

Deleted: re

Deleted:

Deleted: However, d

Deleted: in the control-b run

Deleted: a portion of

Deleted: with non-zero differences in deposition rates between the runs ...

Deleted: due to stronger updrafts again, which are in turn mainly due to more condensation,

Deleted: also start to be higher

Deleted: in the control-b run

Deleted: a portion of

Deleted: with non-zero differences in freezing rates between the runs ...

Deleted: are

Deleted: in the control-b run over most of the altitudes with non-zero differences in deposition rates between the runs

Deleted: are

Deleted: lower

Deleted: over all of altitudes with non-zero differences in freezing rates between the runs

12e). Overall, lower snow and hail mass maintains in the control-b run as time progresses from 17:20 LST to 19:00 LST. As time progresses from 17:20 LST to 19:00 LST, overall higher condensation rates, droplet and raindrop mass maintain in the control-b run (Figure 12e). Here, while the time- and domain-averaged deposition (condensation and freezing) rates are lower (higher) in the control-b run over the whole simulation period, the average differences in freezing rates are ~one to ~two orders of magnitude smaller than those in deposition and condensation rates between the runs. Hence, more condensation (but not deposition and freezing) is a main cause of stronger updrafts in the control-b run. More condensation and more freezing tend to induce increases in the mass of precipitable hydrometeors in the control-b run. Less deposition tends to induce decreases in the mass of precipitable hydrometeors in the control-b run. This competition between condensation, deposition and freezing leads to negligible differences in the cumulative precipitation amount at the last time step between the control-b and low-aerosol-b runs, although roles of freezing in this competition are negligible as compared to those of condensation and deposition.

### c. Condensation frequency distributions, horizontal distributions of condensation and precipitation, and condensation-precipitation correlations

Figure 13 shows the horizontal distribution of the column-averaged condensation rates over the domain and Figure 14 shows the cumulative frequency distributions of column-averaged condensation rates at selected times. As in the Seoul case, the horizontal distribution of condensation rates is superimposed on that of precipitation rates and the terrain in Figure 13. At 14:20 LST, condensation starts to occur in places with mountains, which induce forced convection, and condensation is concentrated around the center of the domain as marked by a yellow circle (Figures 13a and 13b). Note that condensation does not occur in the plain area which is the south of the 100-m terrain-height contour line (Figures 13a and 13b). Due to higher concentrations of aerosols acting as CCN, there is more condensation around the center in the control-b run than in the low-aerosol-b run (Figures 13a and 13b). This leads to a situation where the control-b run has the higher area-

Deleted:

Deleted: the

Deleted: over most of the altitudes with non-zero differences in condensation rates between the runs

Deleted: differences in freezing rates are two to three orders of magnitude smaller than those in condensation and deposition between the runs. Associated with this,

Deleted: and freezing

Deleted: although

Deleted: negligible as compared to

Deleted: deposition

Deleted: Remember that condensation (deposition and freezing) acts as a source of droplets (ice crystals) which are in turn a source of precipitable hydrometeors and precipitation through collision and coalescence processes. Thus,

Deleted: m

Deleted: s

Deleted: the

Deleted: tion

Deleted: rate

Deleted: and freezing

Deleted:

Deleted: tion

Deleted: rate

Deleted: aerosol

averaged condensation rates than the low-aerosol-b run (Figure 12a). Then, as time progresses to 17:20 LST, the condensation area extends to the eastern and western parts of the domain mostly over mountain areas (Figures 13c and 13d). Hence, the main source of condensation is considered to be forced convection over mountains. As seen in Figures 13c and 13d, higher concentrations of aerosols acting as CCN induce the control-b run to have much more condensation spots and thus much bigger areas with condensation than the low-aerosol-b run at 17:20 LST. Associated with this, CCN-induced more condensation in the control-b run maintains with the time progress to 17:20 LST (Figure 12d). At 17:20 LST, precipitation mainly occurs in a spot which is in the western part of areas with relatively high condensation rates (Figures 13c and 13d).

At 17:20 LST, as seen in the cumulative frequency of condensation rates, the control-b run has the higher condensation frequency above condensation rate of  $\sim 10 \times 10^{-3} \text{ g m}^{-3} \text{ s}^{-1}$  and below that of  $\sim 3 \times 10^{-3} \text{ g m}^{-3} \text{ s}^{-1}$  than the low-aerosol-b run (Figure 14a). This pattern of differences in the condensation frequency distribution with the tipping condensation-rate points at  $\sim 10 \times 10^{-3}$  and  $\sim 3 \times 10^{-3} \text{ g m}^{-3} \text{ s}^{-1}$  continues up to 19:00 LST (Figures 14b). Figure 15 shows the mean precipitation rate over each of the column-averaged condensation rates for the period up to 17:20 LST in the control-b run. A column-averaged condensation rate in an air column with a precipitation rate at its surface is obtained and these condensation and precipitation rates are paired at each column and time step. Then, collected precipitation rates are classified and grouped based on the corresponding paired column-averaged condensation rates. The classified precipitation rates corresponding to each of the column-averaged condensation rates are averaged arithmetically to construct Figure 15. There are only less than 10 % differences in the mean precipitation rate for each of the column-averaged condensation rates between the control-b and low-aerosol-b runs (not shown). Figure 15 shows that generally a higher condensation rate is related to a higher mean precipitation rate. It is also roughly shown that, according to the mean precipitation rate for each condensation rate, overall, condensation rates below  $\sim 3 \times 10^{-3} \text{ g m}^{-3} \text{ s}^{-1}$  and above  $\sim 10 \times 10^{-3} \text{ g m}^{-3} \text{ s}^{-1}$  are correlated with precipitation rates below  $\sim 2 \text{ mm hr}^{-1}$  and above  $\sim 12 \text{ mm hr}^{-1}$ , respectively, while condensation rates between  $\sim 3$  and  $\sim 10 \times 10^{-3} \text{ g m}^{-3} \text{ s}^{-1}$  are correlated with precipitation rates between  $\sim 2$  and  $\sim 12 \text{ mm hr}^{-1}$  (Figure 15). Hence, on average, the higher frequency of condensation with rates above  $\sim 10 \times 10^{-3} \text{ g m}^{-3} \text{ s}^{-1}$

Deleted: aerosol

Deleted: aerosol

Deleted: <sup>6</sup>Deleted: <sup>6</sup>Deleted: <sup>6</sup>Deleted: <sup>6</sup>Deleted: <sup>6</sup>Deleted: <sup>6</sup>Deleted: <sup>6</sup>Deleted: <sup>6</sup>

$3 \text{ s}^{-1}$  and below  $\sim 3 \times 10^{-3} \text{ g m}^{-3} \text{ s}^{-1}$  can be considered to lead to the higher frequency of precipitation whose rates are higher than  $\sim 12 \text{ mm hr}^{-1}$  and lower than  $\sim 2 \text{ mm hr}^{-1}$  in the control-b run, respectively. It can also be considered that the lower condensation frequency between  $\sim 3$  and  $\sim 10 \times 10^{-3} \text{ g m}^{-3} \text{ s}^{-1}$  leads to the lower precipitation frequency between  $\sim 2$  and  $\sim 12 \text{ mm hr}^{-1}$  in the control-b run. It is found that this correspondence between condensation and precipitation rates is valid whether analyses to construct Figure 15 are repeated only for a time point at 16:30 LST or for a period between 16:30 and 17:00 LST. These time point and period are related to analyses of the moist static energy as described in Section e below.

At 17:20 LST, the larger precipitation frequency between  $\sim 2$  and  $\sim 12 \text{ mm hr}^{-1}$  in the low-aerosol-b run nearly offsets the larger precipitation frequency in the other ranges of precipitation rates in the control-b run (Figure 11c). This leads to the similar average precipitation rate between the runs at 17:20 LST and contributes to the similar cumulative precipitation at the last time step between the runs (Figure 5b).

#### d. Evaporation and gust fronts

As time progresses from 17:00 to 19:00 LST, the precipitation system moves northward (Figure 16). At the core of the precipitation system, due to evaporation and downdrafts, there is the horizontal outflow forming at 17:00 LST (Figures 16a and 16b). The core is represented by the field of precipitation whose rates are higher than  $1 \text{ mm hr}^{-1}$  in Figure 16. At the core, the northward outflow is magnified by the northward synoptic-scale wind, while at the core, the outflow in the other directions is offset by the northward synoptic-scale wind. Hence, the outflow is mainly northward from 17:00 LST onwards as marked by yellow circles in Figures 16. This enables convergence or a gust front, which is produced by the outflow from the core, to be mainly formed at the north of the core. Note that the intensity of a gust front is proportional to that of outflow from a core of precipitation or convective system (Weisman and Klemp, 1982; Houze, 1993). The strong gust front at the north of the core generates strong updrafts, a significant amount of condensation and precipitation. Then, a subsequent area with clouds and precipitation is formed at the north of the core as time progresses, which means that the precipitation system extends or moves

Deleted: <sup>6</sup>

Deleted:

Deleted: <sup>6</sup>

to the north as seen in comparisons between sub-panels with different times in Figure 16. This movement, which is induced by collaborative work between outflow, synoptic wind and gust fronts, is typical in deep convective clouds.

As described above, the more droplet nucleation and greater integrated droplet surface induce more condensation before 17:00 LST in the control-b run. This and lower efficiency of collision and collection among droplets enable the control-b run to have a larger amount of cloud liquid or droplets as a source of evaporation. This in turn enables more droplet evaporation, more associated cooling and stronger downdrafts, although less rain evaporation is in the control-b run particularly for the period from 17:00 LST to 19:00 LST (Figure 17). More evaporation of droplets and associated stronger downdrafts with higher concentrations of aerosols acting as CCN have been shown by the numerous previous studies (e.g., Tao et al., 2007; Tao et al., 2012; Khain et al., 2008; Lee et al., 2018).

During the period between 17:00 and 19:00 LST, with the development of convergence or the gust front, as mentioned above, the maximum precipitation rate increases from ~ 17 (17) to ~ 45 (33) mm hr<sup>-1</sup> in the control-b (low-aerosol-b) run (Figure 11). This indicates that the gust-front development contributes to the overall intensification of the precipitation system, while it moves northward. If there were only northward synoptic-scale wind with no formation of the gust front, the system would move northward with less intensification. Over the period from 17:00 LST to 19:00 LST, stronger downdrafts and associated stronger outflow generate a stronger gust front and more subsequent condensation in the control-b run. This enhances the small initial difference, which is at 17:00 LST, in the frequency of precipitation with rates above ~12 mm hr<sup>-1</sup> between the runs substantially as time progresses from 17:00 LST to 19:00 LST (Figure 11). Associated with this, with the time progress, the nearly identical maximum precipitation rate between the runs at 17:00 LST turns into the significantly higher maximum precipitation rate in the control-b run than in the low-aerosol-b run (Figure 11). Around 19:00 LST, the system enters its dissipating stage, accompanying reduction in the precipitating area and the area-averaged precipitation rate (Figures 5b, 16m and 16n).

### e. Moist static energy

**Deleted:** During the period between 17:00 and 19:00 LST, the time- and domain-averaged cloud-liquid or droplet evaporation rate is higher and downdrafts are stronger, although the control-b run has the lower average rain evaporation rate than the low-aerosol-b run (Figure 17). This is consistent with the numerous previous studies that have shown more evaporation of droplets and associated stronger downdrafts with higher aerosol concentrations (e.g., Tao et al., 2007; Tao et al., 2012; Khain et al., 2008; Lee et al., 2018).

**Deleted:** Due to higher condensation rates and

**Deleted:** lower autoconversion rates

**Deleted:** ,

**Deleted:** s

**Deleted:** more

**Deleted:** and

**Deleted:** t

**Deleted:** evaporative cooling

**Deleted:** in the control-b run

**Deleted:** . F

**Formatted:** Superscript

**Deleted:** , leading to a situation where the control-b run has

**Deleted:** higher maximum precipitation rate than the low-aerosol-b run. ...

Condensation, which controls droplet mass and precipitation, is controlled by updrafts and updrafts are in turn controlled by instability. One of important factors that maintain instability is the moist static energy. Motivated by this, to better understand differences in the precipitation frequency distribution in association with those in the condensation frequency distribution between the control-b and low-aerosol-b runs, we calculate the flux of the moist static energy and the flux is defined as follows:

$$\vec{F}_S = S \times \rho \times \vec{V} \quad (1),$$

where  $\vec{F}_S$  represents the flux of the moist static energy,  $S$  the moist static energy,  $\rho$  the air density and  $\vec{V}$  the horizontal-wind vector. In Eq. (1), we see that the flux is in the vector form and has two components, which are its magnitude and direction. The fluxes of the moist static energy in the PBL are obtained over the domain at 16:30 LST, since in general, the moist static energy in the PBL has much stronger effects on instability and updrafts than that above the PBL. In particular, we focus on the PBL fluxes of the energy that cross the boundary over a time step at 16:30 LST between areas with the column-averaged condensation rate from  $3 \times 10^{-3} \text{ g m}^{-3} \text{ s}^{-1}$  to  $10 \times 10^{-3} \text{ g m}^{-3} \text{ s}^{-1}$ , which are referred to as “area A”, and those with the column-averaged condensation rate above  $10 \times 10^{-3} \text{ g m}^{-3} \text{ s}^{-1}$ , which are referred to as “area B”. This is because we are interested in the exchange of the moist static energy between areas A and B and this exchange can be seen by looking at those fluxes which cross the boundary between those areas.

We are interested in the exchange of the energy, since we hypothesized that the exchange somehow alters instability in each of areas A and B in a way that there are increases (decreases) in instability, the updraft intensity, condensation and precipitation with increasing concentrations of aerosols acting as CCN in area B (A), leading to the higher (lower) frequency of condensation whose rates are higher than  $10 \times 10^{-3} \text{ g m}^{-3} \text{ s}^{-1}$  (between  $3 \times 10^{-3}$  and  $10 \times 10^{-3} \text{ g m}^{-3} \text{ s}^{-1}$ ) and precipitation whose rates are higher than 12 mm hr<sup>-1</sup> (between 2 and 12 mm hr<sup>-1</sup>) in the control-b run than in the low-aerosol-b run. When the PBL fluxes, which crosses the boundary over the time step at 16:30 LST, are summed at 16:30 LST, there is the net flux from area A to area B. This means that there is the net transportation of the moist static energy from areas with condensation rates between

**Deleted:** Analyses to construct Figure 15 are repeated only for a time point at 16:30 LST and they indicate that as shown in Figure 15 for the period up to 17:20 LST, the column-averaged condensation rates above  $10 \times 10^{-6} \text{ g m}^{-3} \text{ s}^{-1}$  and below  $3 \times 10^{-6} \text{ g m}^{-3} \text{ s}^{-1}$  correspond to precipitation rates above 12 mm hr<sup>-1</sup> and below 2 mm hr<sup>-1</sup>, respectively, at 16:30 LST. According to those analyses, condensation rates between  $3 \times 10^{-6} \text{ g m}^{-3} \text{ s}^{-1}$  and  $10 \times 10^{-6} \text{ g m}^{-3} \text{ s}^{-1}$  correspond to precipitation rates between 2 and 12 mm hr<sup>-1</sup> at 16:30 LST. ....

**Deleted:** as diagrammatically depicted in Figure 18,

**Deleted:** <sup>6</sup>

**Deleted:** <sup>6</sup>

**Deleted:** <sup>6</sup>

**Deleted:** aerosol

**Deleted:** <sup>6</sup>

**Deleted:** <sup>6</sup>

**Deleted:**  $\text{g m}^{-3} \text{ s}^{-1}$

**Deleted:** <sup>6</sup>

**Deleted:** averaged over the domain



$3 \times 10^{-3}$  and  $10 \times 10^{-3} \text{ g m}^{-3} \text{ s}^{-1}$  to those with condensation rates greater than  $10 \times 10^{-3} \text{ g m}^{-3} \text{ s}^{-1}$  in the PBL at 16:30 LST as shown in Table 2. Table 2 shows the **net summed** flux of the moist static energy which crosses the boundary between areas A and B in the control-b run as well as the low-aerosol-b run. To calculate the **net** flux at 16:30 LST in Table 2, the fluxes, which cross the boundary between areas A and B over the time step at 16:30 LST, only at grid points in the PBL are summed. For the calculation, the flux from area A to area B has a positive sign, while the flux from area B to area A has a negative sign. Since the **net** flux is positive for both of the runs **as shown in Table 2**, there is the net flux from area A to area B in the PBL. The above-described analysis for the fluxes crossing the boundary between areas A and B is repeated for every time step between 16:30 and 17:00 LST and based on this, the **net summed** flux over the period between 16:30 and 17:00 LST is obtained. As shown in Table 2, the **net** flux for the period between 16:30 and 17:00 LST is also positive as in the situation only for 16:30 LST. This means, **that** there is the net transportation of the moist static energy from area A to area B in the PBL during the period between 16:30 and 17:00 LST.

At 16:30 LST, condensation with rates above  $10 \times 10^{-3} \text{ g m}^{-3} \text{ s}^{-1}$  starts to develop and this forms area B. Area B has stronger updrafts via greater condensational heating than in other areas, including area A, with lower condensation rates. Stronger updrafts in area B induce the convergence of air and associated moist static energy from area A to area B. Since the average condensation rate and updrafts at 16:30 LST over area B are higher and stronger due to increasing concentrations **of aerosols acting as CCN**, respectively, the air convergence and the associated transportation of the moist static energy in the PBL from area A to area B are stronger and more, respectively, in the control-b run than in the low-aerosol-b run (Table 2). Stated differently, area B steals the moist static energy from area A, and this occurs more effectively in the control-b run. This increases instability and further intensifies updrafts in area B, and decreases instability and weakens updrafts in area A, while these increases and decreases (intensification and weakening) of instability (updrafts) are greater in the control-b run for the period from 16:30 **LST** to 17:00 LST. This increases condensation, cloud mass and precipitation whose rates are higher than 12 mm hr<sup>-1</sup> in area B, and decreases condensation, cloud mass and precipitation whose rates are from 2 **mm hr<sup>-1</sup>** to 12 mm hr<sup>-1</sup> in area A. These increases and decreases occur more

Deleted: <sup>6</sup>Deleted:  $\text{g m}^{-3} \text{ s}^{-1}$ Deleted: <sup>6</sup>Deleted: <sup>6</sup>

Deleted: average

Deleted:

Deleted: average

Deleted: and divided by the number of all grid points over the whole domain at 16:30 LST. Here, all grid points include grid points with those fluxes crossing the boundary and those without those fluxes including grid points with zero fluxes, and include grid points both in and above the PBL.

Deleted: as depicted in Figure 18

Deleted: average

Deleted: on average,

Deleted: the average of

Deleted: average

Deleted: Analyses to construct Figure 15 are repeated again for a time period between 16:30 and 17:00 LST. These repeated analyses find that as in the situation only for 16:30 LST, the column-averaged condensation rates below  $3 \times 10^{-6} \text{ g m}^{-3} \text{ s}^{-1}$  and above  $10 \times 10^{-6} \text{ g m}^{-3} \text{ s}^{-1}$  correspond to precipitation rates below 2 mm hr<sup>-1</sup> and above 12 mm hr<sup>-1</sup>, respectively, while the column-averaged condensation rates between  $3 \times 10^{-6} \text{ g m}^{-3} \text{ s}^{-1}$  and  $10 \times 10^{-6} \text{ g m}^{-3} \text{ s}^{-1}$  correspond to precipitation rates between 2 and 12 mm hr<sup>-1</sup> for every time step between 16:30 and 17:00 LST.

Deleted: average

Deleted: on average

Deleted: ,

Deleted: <sup>6</sup>

Deleted: aerosol



effectively for the control-b run than for the low-aerosol-b run during the period. This in turn leads to the lower precipitation frequency for the precipitation rates from 2 mm hr<sup>-1</sup> to 12 mm hr<sup>-1</sup> and the higher frequency for the precipitation whose rates are higher than 12 mm hr<sup>-1</sup> at 17:00 LST in the control-b run (Figure 11b). The weakened updrafts and reduced condensation turn a portion of precipitation with rates between 2 and 12 mm hr<sup>-1</sup> to precipitation whose rates are below 2 mm hr<sup>-1</sup>, and this takes place more efficiently in the control-b run during the period between 16:30 and 17:00 LST. This eventually increases the frequency of precipitation rates below 2 mm hr<sup>-1</sup> and this increase is greater for the control-b run, leading to the greater precipitation frequency for the precipitation rates below 2 mm hr<sup>-1</sup> in the control-b run at 17:20 LST (Figure 11c).

## 5. Discussion

### 5.1 Comparison of the Seoul and Beijing cases

In this section, we compare the Seoul case to the Beijing case. For the comparison, remember that on average, a pair of the control-s and low-aerosol-s runs has the same perturbation of aerosols acting as CCN as in a pair of the control-b and low-aerosol-b runs. Associated with the fact that clouds in the Seoul case are less deep than those in the Beijing case, overall, updrafts in the Seoul case are not as strong as those in the Beijing case. Hence, unlike the situation in the Beijing case, stronger updrafts, which accompany higher condensation rates, and associated convergence in the Seoul case are not strong enough to steal the sufficient amount of the moist static energy from weaker updrafts which accompany lower condensation rates. This makes the redistribution of the moist static energy between areas with relatively higher condensation rates and those with relative lower condensation rates, such as that between areas A and B for the Beijing case, ineffective for the Seoul case. Due to this, the sign of CCN-induced changes in the frequency of precipitation rates does not vary throughout all of the precipitation rates except for the range of low precipitation rates where there are nearly no CCN-induced changes in the frequency in the Seoul case as shown in Figure 6a. As seen in Figure 6a, mainly due to increases in condensation and deposition, precipitation frequency increases

Deleted:

**Deleted:** To examine aerosol effects on the Beijing case, the control-b and the low-aerosol-b runs are compared, and remember that the low-aerosol-b run is the repeated control-b run by simply reducing the background-aerosol concentrations at each of grid points and time steps by a factor of 3.1. Remember that the low-aerosol-s run is the repeated control-s run and the low-aerosol-s run has the 3.1 times lower concentration of background aerosols, which is averaged over the whole domain and simulation period, than the control-s run. Hence, the relative variation of the average concentration of background aerosols from the control-b run to the low-aerosol-b run is not different from that from the control-s run to the low-aerosol-s run. This enables the two pairs of runs to be compared for an identical magnitude of an aerosol perturbation. ¶

**Deleted:** Note

**Deleted:** as compared to

**Deleted:** . Thus,

**Deleted:** clouds and associated

**Deleted:** aerosol

**Deleted:** aerosol

for most of precipitation rates, although the precipitation frequency does not show significant changes as concentration of aerosols acting as CCN increases for relatively low precipitation rates in the control-s run as compared to that in the low-aerosol-s run. This means that there are no tipping precipitation rates where the sign of CCN-induced changes in the frequency of precipitation rates changes in the Seoul case, contributing to the higher cumulative precipitation amount in the simulation with higher concentrations of aerosols acting as CCN for the Seoul case, which are different from the situation in the Beijing case.

In the Beijing case with deeper clouds as compared to those in the Seoul case, clouds develop gust fronts via strong downdrafts and associated strong outflow. These gust fronts play an important role in developing strong convection and associated high precipitation rates. Unlike the situation in the Seoul case, there are strong clouds and associated updraft entities that are able to steal heat and moisture (or the moist static energy) as sources of instability from areas with relatively less strong clouds and updrafts with medium strength;

note that these strong clouds here involve stronger updrafts via greater condensational heating as described in Section e above and this enables these clouds to be thicker and have higher cloud mass than these less strong clouds. This further intensifies strong clouds and weakens less strong clouds with medium strength. Due to this, the cumulative frequency

of heavy (medium) precipitation in association with strong clouds (less strong clouds with medium strength) increases (decreases). Some of the weakened clouds eventually produce light precipitation, which increase the cumulative frequency for light precipitation. The intensification of strong clouds and the weakening of less strong clouds with medium strength gets more effective with increasing concentration of aerosols acting as CCN.

Hence, in the Beijing case, for medium precipitation in association with less strong clouds, the simulation with higher concentration of aerosols acting as CCN shows the lower cumulative precipitation frequency at the last time step. However, for heavy precipitation, which is associated with strong clouds, and light precipitation, the simulation with higher concentrations of aerosols acting as CCN shows the higher cumulative precipitation frequency at the last time step. These differential responses of precipitation to increasing

concentration of aerosols acting as CCN among different types of precipitation occur in the circumstances of the similar cumulative precipitation amount between the simulations with different concentration of aerosols acting as CCN. This similar precipitation amount is due

Deleted: aerosol

Deleted: aerosol

Deleted: aerosol

Deleted: .

Deleted:

Deleted: aerosol

Deleted: s

Deleted: with medium strength

Deleted: aerosol

Deleted: s

Deleted: aerosol

Deleted: aerosol

Deleted: s

Deleted: aerosol

Deleted: s

to above-mentioned competition between CCN-induced changes in condensation, deposition and freezing.

In both of the Seoul and Beijing cases, CCN-induced changes in condensation plays an important role in making differences in the precipitation amount and/or the precipitation frequency distribution between the simulations with different concentration of aerosols acting as CCN. It is notable that in less deep clouds in the Seoul case, in addition to condensation, deposition plays a role in precipitation to induce CCN-induced increases in the precipitation amount. CCN-induced increases in condensation initiate the differences in cloud mass and precipitation and then CCN-induced increases in deposition follow to further enhance those differences. In deep clouds in the Beijing case, condensation tends to induce increases in cloud mass and precipitation, while deposition tends to induce decreases in cloud mass and precipitation with increasing concentration of aerosols acting as CCN. Hence, as clouds get shallower and thus ice processes become less active, the role of deposition in CCN-induced changes in precipitation amount turns from CCN-induced suppression of precipitation to enhancement of precipitation. Here, we find that contrary to the traditional understanding, the role of variation of freezing, which is induced by the varying concentration of aerosols acting as CCN but not INPs, in precipitation is negligible, as compared to that of condensation and deposition in both of the cases.

## 6. Summary and conclusions

This study examines impacts of aerosols, which act as CCN, on clouds and precipitation in two metropolitan areas, which are the Seoul and Beijing areas, in East Asia that has experienced substantial increases in aerosol concentrations over the last decades. The examination is performed via simulations, which use a CSRM. These simulations are for deep clouds which reach the tropopause in the Beijing case and for comparatively less deep clouds which do not reach the tropopause yet grow above the level of freezing in the Seoul case.

In both of the cases, CCN-induced changes in condensation plays a critical role in CCN-induced variation of precipitation properties (e.g., the precipitation amount and the precipitation frequency distribution). In the Seoul case, CCN-induced increases in

Deleted: aerosol

Deleted: aerosol

Deleted: aerosol

Deleted: s

Deleted: aerosol

Deleted: Aerosol

Deleted: aerosol

Deleted:

Deleted: However, i

Deleted:

Deleted: s

Deleted: with increasing aerosol concentrations

Deleted: aerosol

Deleted: s

Deleted: ice processes

Deleted: aerosol

Deleted: aerosol

Deleted:

Deleted: aerosol-induced

Deleted: not significant

Deleted: that of condensation and deposition in

Deleted: both of the cases

Deleted: aerosol

Deleted: aerosol

Deleted: aerosol

condensation and subsequent increases in deposition lead to CCN-induced increases in the precipitation frequency over most of precipitation rates and thus in the precipitation amount. However, in the Beijing case, while there are increases in condensation with increasing CCN concentrations, there are decreases in deposition with increasing CCN concentrations. This competition between increases in condensation and decreases in deposition leads to negligible CCN-induced changes in cumulative precipitation amount in the Beijing case. In both of the cases, CCN-induced changes in freezing are negligible as compared to those in condensation and deposition. In the Beijing case, there is another competition for the moist static energy among clouds with different updrafts and condensation. This competition results in CCN-induced differential changes in the precipitation frequency distributions. With clouds getting deeper from the Seoul case to the Beijing case, clouds and associated updrafts, which are strong enough to steal the moist static energy from other clouds and their updrafts, appear. This makes strong clouds stronger and clouds with medium strength weaker. With higher CCN concentrations, strong clouds steal more energy, and thus strong clouds become stronger and clouds with medium strength weaker with a greater magnitude. As a result of this, there are more frequent heavy precipitation (whose rates are higher than  $12 \text{ mm hr}^{-1}$ ) and light precipitation (whose rates are lower than  $2 \text{ mm hr}^{-1}$ ), and less frequent medium precipitation (with rates from  $2 \text{ mm hr}^{-1}$  to  $12 \text{ mm hr}^{-1}$ ) with increasing CCN concentrations in the Beijing case.

In both of the Seoul and Beijing cases, there are mountains and they play an important role in how cloud and precipitation evolve with time and space. In both of the cases, the precipitating system moves or expands over mountains which induce forced convection and generate condensation. This important role of mountains and forced convection in the formation and evolution of the precipitation system has not been examined much in the previous studies of aerosol-cloud interactions, since many of those previous studies (e.g., Jiang et al., 2006; Khain et al., 2008; Li et al., 2011; Morrison et al., 2011) have dealt with convective clouds that develop over plains and oceans. Hence, findings in this study, which are related to mountain-forced convection and its interactions with aerosols, can be complementary to those previous studies. Stated differently, this study can shed light on our path to the understanding of aerosol-cloud interactions over more general domains not only with no terrain but also with terrain.

Deleted: aerosol

Deleted: ; note that condensation and deposition are sources of cloud mass and precipitation.

Deleted:

Deleted: aerosol

Deleted: aerosol

Deleted: So, there is competition between increases in condensation and decreases in deposition.

Deleted: s

Deleted: aerosol

Deleted:

Deleted: Also

Deleted: in the Beijing case

Deleted: aerosol

Deleted: 1

Deleted: aerosol

Deleted: the

Deleted: aerosol

### Code/Data availability

Our private computer system stores the code/data which are private and used in this study. Upon approval from funding sources, the data will be opened to the public. Projects related to this paper have not been finished, thus, the sources prevent the data from being open to the public currently. However, if information on the data is needed, contact the corresponding author Seoung Soo Lee (slee1247@umd.edu).

### Author contributions

Essential initiative ideas are provided by SSL, KJH and KHS to start this work. Simulation and observation data are analyzed by SSL, JC and GK. JU and YZ review the results and contribute to their improvement. CHJ and JG perform additional simulations, which are required by the review process, and their basic analyses. CHJ also provide ideas to handle the reviewers' comments.

### Competing interests

The authors declare that they have no conflict of interest.

### Acknowledgements

This study is supported by the National Research Foundation of Korea (NRF) grant funded by the Korea government (MSIT) (No. NRF2020R1A2C1003215) and the “Construction of Ocean Research Stations and their Application Studies” project funded by the Ministry of Oceans and Fisheries, South Korea. This study is also supported by the National Research Foundation of Korea (NRF) by FRIEND (Fine Particle Research Initiative in East Asia Considering National Differences) project through the National Research Foundation of Korea (NRF) funded by the Ministry of Science and ICT (2020M3G1A1114617). Authors thank Danhong Dong at Chinese Academy of Sciences and Fang Wu at Beijing Normal University for their reviewing this paper.

Deleted: ¶

Formatted: Font: (Asian) Times New Roman, Bold

Formatted: Font: Bold

Deleted: ed

Deleted: ed

Deleted: .

Formatted: Font: (Default) Batang, (Asian) Batang

Deleted: ,

## References

- [Brown, A., Milton, S., Cullen, M., Golding, B., Mitchell, J., and Shelly, A.: Unified modeling and prediction of weather and climate: A 25-year journey, \*Bull. Am Meteorol. Soc.\* \*\*93\*\*, 1865–1877, 2012.](#)
- Chen, F., and Dudhia, J.: Coupling an advanced land-surface hydrology model with the Penn State-NCAR MM5 modeling system. Part I: Model description and implementation, *Mon. Wea. Rev.*, **129**, 569–585, 2001.
- Dong, B., Wilcox, L. J., Highwood, E. J., and Sutton, R. T.: Impacts of recent decadal changes in Asian aerosols on the East Asian summer monsoon: roles of aerosol–radiation and aerosol–cloud interactions, *Clim. Dyn.*, **53**, 3235–3256, 2019.
- Eun, S.-H., Kim, B.-G., Lee, K.-M., and Park, J.-S.: Characteristics of recent severe haze events in Korea and possible inadvertent weather modification, *SOLA*, **12**, 32–36, 2016.
- Fan, J., Yuan, T., Comstock, J. M., et al.: Dominant role by vertical wind shear in regulating aerosol effects on deep convective clouds, *J. Geophys. Res.*, **114**, doi:10.1029/2009JD012352, 2009.
- Fouquart, Y., and Bonnel, B.: Computation of solar heating of the Earth's atmosphere: a new parameterization, *Beitr. Phys. Atmos.*, **53**, 35–62, 1980.
- Ha, K.-J., Nam, S., Jeong, J.-Y., et al.: Observations utilizing Korean ocean research stations and their applications for process studies, *Bull. Amer. Meteor. Soc.*, **100**, 2061–2075, 2019.
- Holben, B. N., Tanré, D., Smirnov, et al.: An emerging ground-based aerosol climatology: Aerosol optical depth from AERONET, *J. Geophys. Res.*, **106**, 12067–12097, 2001.
- Houze, R. A., Cloud dynamics, Academic Press, 573 pp, 1993.
- Hwang, S.-O., and Lee, D.-K.: A study on the relationship between heavy rainfalls and associated low-level jets in the Korean peninsula, *J. Korean. Meteorol. Soc.*, **29**, 133–146, 1993.
- Jiang, H., Xue, H., Teller, A., Feingold, G., and Levin, Z.: Aerosol effects on the lifetime of shallow cumulus, *Geophys. Res. Lett.*, **33**, L14806, doi:10.1029/2006GL026024, 2006.

Deleted: ¶

- 1490 Kar, S. K., Lioi, Y.A., and Ha, K.-J. : Aerosol effects on the enhancement of cloud-to-  
 1491 ground lightning over major urban areas of South Korea, Atmos. Res. , 92, 80-87,  
 1492 2009.
- 1493 Khain, A., BenMoshe, N., and Pokrovsky, A.: Factors determining the impact of aerosols  
 1494 on surface precipitation from clouds: Attempt of classification, J. Atmos. Sci., 65,  
 1495 1721-1748, 2008.
- 1496 Khain, A., Pokrovsky, A., Rosenfeld, D., Blahak, U., and Ryzhkoy, A.: The role of CCN in  
 1497 precipitation and hail in a mid-latitude storm as seen in simulations using a spectral  
 1498 (bin) microphysics model in a 2D dynamic frame, Atmos. Res., 99, 129–146, 2011.
- 1499 Khain, A., Rosenfeld, D., and Pokrovsky, A.: Aerosol impact on the dynamics and  
 1500 microphysics of deep convective clouds, Quart. J. Roy. Meteor. Soc., 131, 2639-266,  
 1501 2005.
- 1502 Khain, A. D., BenMoshe, N., and A. Pokrovsky, A.: Factors determining the impact of  
 1503 aerosols on surface precipitation from clouds: An attempt at classification, J. Atmos.  
 1504 Sci., 65, 1721–1748, doi:10.1175/2007JAS2515.1, 2008.
- 1505 King, J.: Automatic weather stations, available at  
 1506 [https://web.archive.org/web/20090522121225/http://www.automaticweatherstation.c](https://web.archive.org/web/20090522121225/http://www.automaticweatherstation.com/index.html)  
 1507 [om/index.html](https://web.archive.org/web/20090522121225/http://www.automaticweatherstation.com/index.html), 2009.
- 1508 Koop, T., Luo, B. P., Tsias, A., and Peter, T.: Water activity as the determinant for  
 1509 homogeneous ice nucleation in aqueous solutions, Nature, 406, 611-614, 2000.
- 1510 Lebo, Z. J., and Morrison, H.: Dynamical effects of aerosol perturbations on simulated  
 1511 idealized squall lines, Mon. Wea. Rev., 142, 991-1009, 2014.
- 1512 Lee, D.-K., Kim, H.-R., and Hong, S.-Y.: Heavy rainfall over Korea during 1980–1990.  
 1513 Korean, J. Atmos. Sci., 1, 32–50, 1998.
- 1514 Lee, S., Ho, C.-H., Lee, Y. G., Choi, H.-J. and Song, C.-K.: Influence of transboundary air  
 1515 pollutants from China on the high-PM10 episode in Seoul, Korea for the period  
 1516 October 16–20, 2008. Atmos. Environ., 77, 430–439, 2013.
- 1517 Lee, S. S., Donner, L. J., Phillips, V. T. J., and Ming, Y.: The dependence of aerosol effects  
 1518 on clouds and precipitation on cloud-system organization, shear and stability, J.  
 1519 Geophys. Res., 113, D16202, 2008.
- 1520 Lee, S. S., Kim, B.-G., and Yum, S. S., et al.: Effect of aerosol on evaporation, freezing and

**Formatted:** Font: (Default) Times New Roman, (Asian) Malgun Gothic, 12 pt, Font color: Black

**Formatted:** Indent: Left: 0", Hanging: 2 ch

**Formatted:** Font: (Asian) Malgun Gothic, Font color: Black

**Formatted:** Font: (Asian) Malgun Gothic, Font color: Black

**Formatted:** Font: (Asian) Malgun Gothic, Font color: Black

**Formatted:** Font: (Asian) Malgun Gothic, Font color: Black

**Formatted:** Font: (Asian) Malgun Gothic, Not Italic, Font color: Black

**Formatted:** Font: (Asian) Malgun Gothic, Font color: Black

- precipitation in a multiple cloud system, *Clim. Dyn.*, 48, 1069-1087, 2016.
- Lee, S. S., Li, Z., Mok, J., et al.: Interactions between aerosol absorption, thermodynamics, dynamics, and microphysics and their impacts on clouds and precipitation in a multiple-cloud system, *Clim. Dyn.*, <https://doi.org/10.1007/s00382-017-3552-x>, 2017.
- Lee, S. S., Kim, B.-G., Li, Z., Choi, Y.-S., Jung, C.-H., Um, J., Mok, J., and Seo, K.-H.: Aerosol as a potential factor to control the increasing torrential rain events in urban areas over the last decades, *Atmos. Chem. Phys.*, 18, 12531–12550, <https://doi.org/10.5194/acp-18-12531-2018>, 2018.
- Li, Z., Niu, F., Fan, J., Liu, Y., Rosenfeld, D., and Ding, Y.: Long-term impacts of aerosols on the vertical development of clouds and precipitation, *Nat. Geosci.*, 4, 888-894, 2011.
- Lohmann, U. and Diehl, K.: Sensitivity studies of the importance of dust ice nuclei for the indirect aerosol effect on stratiform mixed-phase clouds, *J. Atmos. Sci.*, 63, 968-982, 2006,
- Lu, Z., Zhang, Q., and Streets, D. G.: Sulfur dioxide and primary carbonaceous aerosol emissions in China and India, 1996–2010, *Atmos. Chem. Phys.*, 11, 9839–9864, 2011.
- Mlawer, E. J., Taubman, S. J., Brown, P. D., Iacono, M. J., and Clough, S. A.: RRTM, a validated correlated-k model for the longwave, *J. Geophys. Res.*, 102, 16663-1668, 1997.
- Möhler, O., et al, Efficiency of the deposition mode ice nucleation on mineral dust particles, *Atmos. Chem. Phys.*, 6, 3007-3021, 2006.
- Morrison, H., and Grabowski, W. W.: Cloud-system resolving model simulations of aerosol indirect effects on tropical deep convection and its thermodynamic environment, *Atmos. Chem. Phys.*, 11, 10503–10523, 2011.
- Oh, H., Ha, K.-J. and Timmermann, A.: Disentangling Impacts of Dynamic and Thermodynamic Components on Late Summer Rainfall Anomalies in East Asia, *J. Geophys. Res.*, 123, 8623-8633, 2018.
- Oh, H.-R., Ho, C.-H., Kim, J., Chen, D., Lee, S., Choi, Y.-S., Chang, L.-S., and Song, C.-K.: Long-range transport of air pollutants originating in China: A possible major cause of multi-day high-PM10 episodes during cold season in Seoul, Korea. *Atmos.*

Formatted: Font: Not Italic

Formatted

Formatted: Font: (Asian) Malgun Gothic, Font color: Black

Formatted: Font: (Default) Times New Roman, (Asian) Malgun Gothic, Not Italic, Font color: Black

Formatted: Font: (Asian) Malgun Gothic, Font color: Black



1552 Environ., 109, 23–30, 2015.  
 1553 Pruppacher, H. R. and Klett, J. D.: Microphysics of clouds and precipitation, 714pp, D.  
 1554 Reidel, 1978.  
 1555 Rosenfeld, D., Lohmann, U., Raga, G. B., et al.: Flood or drought, How do aerosols affect  
 1556 precipitation? Science, 321, 1309-1313, 2008.  
 1557 Storer, R. L., van den Heever, S. C., and Stephens, G. L.: Modeling aerosol impacts on  
 1558 convection under differing storm environments, J. Atmos. Sci., 67, 3904-3915, 2010.  
 1559 Seo, K.-H., Son, J. H., Lee, J.-H., and Park, H.-S.: Northern East Asian monsoon  
 1560 precipitation revealed by air mass variability and its prediction, J. Clim., 28, 6221-  
 1561 6233, 2013.  
 1562 Tao, W.-K., Chen, J.-P., Li, Z., Wang, C., and Zhang, C.: Impact of aerosols on convective  
 1563 clouds and precipitation, Rev. Geophys., 50, RG2001, 2012.  
 1564 Tao, W. K., Cloud resolving modeling, J. Meteorol. Soc. Jpn., 85B, 305–330,  
 1565 doi:10.2151/jmsj.85B.305, 2007.  
 1566 van den Heever, S. C., Carrió, G. G., Cotton, W. R., DeMott, P. J., and Prenni, A. J.:  
 1567 Impacts of nucleating aerosol on Florida storms. part I: Mesoscale simulations, J.  
 1568 Atmos. Sci., 63, 1752–1775, 2006.  
 1569 Wang, H., Skamarock, W. C., and Feingold, G.: Evaluation of scalar advection schemes in  
 1570 the Advanced Research WRF model using large-eddy simulations of aerosol-cloud  
 1571 interactions, Mon. Wea. Rev., 137, 2547-2558, 2009.  
 1572 Weisman, M. L., and Klemp, J. B.: The dependence of numerically simulated convective  
 1573 storms on vertical wind shear and buoyancy, Mon. Wea. Rev., 110, 504-520, 1982.  
 1574  
 1575  
 1576  
 1577  
 1578  
 1579  
 1580  
 1581  
 1582  
 1583  
 1584  
 1585  
 1586

## FIGURE CAPTIONS

Figure 1. Wind ( $\text{m s}^{-1}$ ), equivalent potential temperature (K), and geopotential height (m) at 850 hPa level over Northeast Asia at (a) 21:00 LST December 23<sup>rd</sup> 2017 and (b) 09:00 LST July 27<sup>th</sup> 2015. Wind, equivalent potential temperature, and geopotential height are represented by arrows, a shaded field, and contours, respectively. An inner rectangle in the Korean Peninsula in (a) marks the Seoul area and that in the East-Asia continent in (b) marks the Beijing area.

Figure 2. Inner rectangles in (a) and (b) mark the Seoul area in the Korean Peninsula and the Beijing area in the East-Asia continent, respectively. A dot outside the inner rectangle in (a) marks Baekryongdo island. Dots in the inner rectangles in (a) and (b) mark the selected locations where precipitation and aerosol mass are measured. In (a) and (b), the light blue represents the ocean and the green the land area.

Figure 3. Surface size distribution of aerosols (a) for the Seoul case and (b) for the Beijing case. Aerosol number concentration per unit volume of air is represented by N and aerosol diameter by D.

Figure 4. Time series of  $\text{PM}_{2.5}$  observed at the ground station in Baekryongdo island (blue line) and of the average  $\text{PM}_{2.5}$  over ground stations in the Seoul area (red line) between 07:00 LST on December 22<sup>nd</sup> and 21:00 LST on December 24<sup>th</sup> in 2017. Note that  $\text{PM}_{2.5}$  observed at stations in the Seoul area is applied to the control-s run whose period is marked by the dashed rectangle. Time series of the average  $\text{PM}_{2.5}$  over stations in the Seoul area in the low-aerosol-s run for the simulation period is also shown (black solid line).

Figure 5. Time series of precipitation rates at the surface, which are averaged over the domain and smoothed over 1 hour, (a) for the control-s and low-aerosol-s runs in the Seoul area and (b) for the control-b and low-aerosol-b runs in the Beijing area. In (a) and (b), the

Deleted: ¶

Deleted: at 850 hPa level

Deleted:

Deleted: The

Deleted: R

Deleted: in (a)

1642 averaged and observed precipitation rates over the observation sites in the Seoul and  
1643 Beijing areas, respectively, are also shown.

1644

1645 Figure 6. Observed and simulated cumulative frequency distributions of precipitation rates  
1646 at the surface for (a) the Seoul case, which are collected over the Seoul area, and (b) the  
1647 Beijing case, which are collected over the Beijing area, at the last time step. Simulated  
1648 distributions are in the control-s and low-aerosol-s runs for the Seoul case and in the  
1649 control-b and low-aerosol-b runs for the Beijing case. The observed distribution is obtained  
1650 by interpolating and extrapolating the observed precipitation rates to grid points and time  
1651 steps in the control-s and control-b runs for the Seoul and Beijing cases, respectively.

1652

1653 Figure 7. Cumulative frequency distributions of the precipitation rates at the surface in the  
1654 control-s and low-aerosol-s runs for the Seoul case at (a) 06:00, (b) 10:00 and (c) 12:00  
1655 LST.

1656

1657 Figure 8. Vertical distributions of differences in the area-averaged condensation,  
1658 deposition and freezing rates, and cloud-liquid, raindrop, snow and hail mass density, and  
1659 updraft mass fluxes between the control-s and low-aerosol-s runs at (a) 03:20, (b) 03:40,  
1660 (c) 06:00 and (d) 12:00 LST. The horizontal black line in each panel represents the altitude  
1661 of freezing or melting. Here, for the sake of the display brevity, snow mass density includes  
1662 ice-mass density, while hail mass density includes graupel mass density.

1663

1664 Figure 9. Spatial distributions of terrain heights, column-averaged condensation rates,  
1665 surface wind vectors and precipitation rates at (a) and (b) 03:40, (c) and (d) 07:20, (e) and  
1666 (f) 08:40, (g) and (h) 10:00, (i) and (j) 11:00, and (k) and (l) 12:00. The distributions in the  
1667 control-s run are shown in (a), (c), (e), (g), (i) and (k), and the distributions in the low-  
1668 aerosol-s run are shown in (b), (d), (f), (h), (j) and (l). Condensation rates are shaded. Dark-  
1669 yellow and dark-red contours represent precipitation rates at 0.5 and 3.0 mm hr<sup>-1</sup>,  
1670 respectively, while beige, light brown and brown contours represent terrain heights at 100,  
1671 300 and 600 m, respectively. See text for yellow rectangles in (a), (b), (g) and (h)

1672

Deleted: (b) 07:20, (c) 09:00,

Deleted: d

Deleted: e

Deleted: and

Deleted: and

Deleted: at the surface

Deleted: , (c) and (d) 06:20

Deleted: e

Deleted: f

Deleted: (g) and (h) 08:00, (i) and (j) 08:20,

Deleted: k

Deleted: l

Deleted: , (m) and (n) 09:00

Deleted: o

Deleted: p

Deleted: , (q) and (r) 10:20

Deleted: s

Deleted: t

Deleted: u

Deleted: v

Deleted: , (w) and (x) 13:00, (y) and (z) 15:20 LST

Deleted: (g), (i),

Deleted: k

Deleted: m

Deleted: ,

Deleted: o

Deleted: , (q), (s), (u),

Deleted: (w) and (y),

Deleted: ,

Deleted: , (n), (p), (r), (t), (v), (x) and (z).

Deleted: o

Deleted: p

Figure 10. Cumulative frequency distributions of the column-averaged condensation rates in the control-s and low-aerosol-s runs for the Seoul case at (a) 07:20 and (b) 09:00 LST.

Figure 11. Cumulative frequency distributions of the precipitation rates at the surface in the control-b and low-aerosol-b runs for the Beijing case at (a) 16:00, (b) 17:00, (c) 17:20, and (d) 19:00 LST.

Figure 12. Same as Figure 8 but for differences between the control-b and low-aerosol-b runs at (a) 14:20, (b) 15:40, (c) 16:00, (d) 17:20 and (e) 19:00 LST.

**Deleted:** Vertical distributions of differences in the area-averaged condensation, deposition and freezing rates, and cloud-liquid and snow mass density, and updraft mass fluxes

Figure 13. Spatial distributions of terrain heights, column-averaged condensation rates, surface wind vectors and precipitation rates at (a) and (b) 14:20, and (c) and (d) 17:20 LST.

**Deleted:** ¶

(a) and (c) are for the control-b run and (b) and (d) are for the low-aerosol-b run. Condensation rates are shaded. Dark-yellow and dark-red contours represent precipitation rates at 1.0 and 2.0 mm hr<sup>-1</sup>, respectively, while beige, light brown, brown and dark brown contours represent terrain heights at 100, 500, 1000 and 1500 m, respectively. See text for yellow circles in (a) and (b).

**Deleted:** and

**Deleted:** at the surface

Figure 14. Cumulative frequency distributions of the column-averaged condensation rates in the control-b and low-aerosol-b runs for the Beijing case at (a) 17:20 and (b) 19:00 LST.

**Deleted:** Yellow circles in (a) and (b) mark places where most of condensation occurs. ¶

Figure 15. Mean precipitation rates corresponding to each column-averaged condensation rate for the period between 14:00 and 17:20 LST in the control-b run. One standard deviation of precipitation rates is represented by a vertical bar at each condensation rate.

**Deleted:** for

Figure 16. Spatial distributions of precipitation rates (shaded) and wind vectors (arrows) for the Beijing case at (a) and (b) 17:00, (c) and (d) 17:20, (e) and (f) 17:40, (g) and (h) 18:00, (i) and (j) 18:20, (k) and (l) 18:40, and (m) and (n) 19:00 LST. The distributions in the control-b run are in (a), (c), (e), (g), (i), (k) and (m). The distributions in the low-aerosol-b run are in (b), (d), (f), (h), (j), (l) and (n).

Figure 17. Vertical distributions of (a) the area-averaged cloud-liquid and rain evaporation rates and (b) downdraft mass fluxes in the control-b and low-aerosol-b runs over a period from 17:00 to 19:00 LST.

**Deleted:** Figure 18. Diagram that depicts the flux of the moist static energy (arrows) between area A (blue) and area B (red). See text for details.

**Deleted:**

**Deleted:**

Simulations	Site	Concentrations of background aerosols acting as CCN
Control-s run	Seoul area	Observed and affected by the aerosol advection
Low-aerosol-s run	Seoul area	Same as those in the control-s run but unaffected by the aerosol advection
Control-b run	Beijing area	Observed
Low-aerosol-b run	Beijing area	Reduced by a factor of 3.1 as compared to those observed

Table 1. Summary of simulations

Simulations	The <del>net</del> flux of the moist static energy which crosses the boundary between areas A and B ( $\text{J m}^{-2} \text{s}^{-1}$ )	
	At 16:30 LST	16:30 to 17:00 LST
Control-b run	$1.57 \times 10^{12}$	$1.07 \times 10^{15}$
Low-aerosol-b run	$1.15 \times 10^{12}$	$7.55 \times 10^{14}$

Table 2. ~~The net~~ flux of the moist static energy which crosses the boundary between areas A and B at 16:30 LST and for a period from 16:30 to 17:00 LST.

- Deleted: average
- Deleted: 5
- Deleted: 5
- Deleted: 5
- Deleted: 1
- Deleted: 5
- Deleted: 1.2
- Deleted: 5
- Deleted: Average

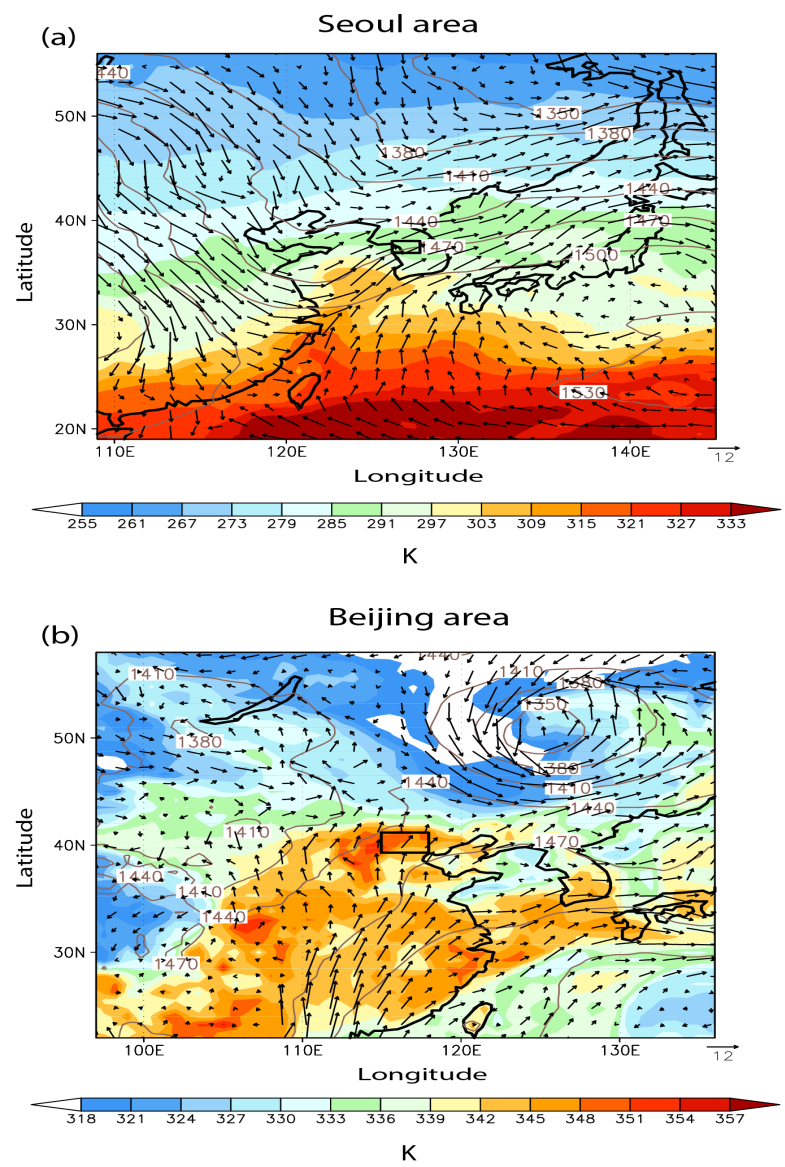


Figure 1

1806  
1807  
1808

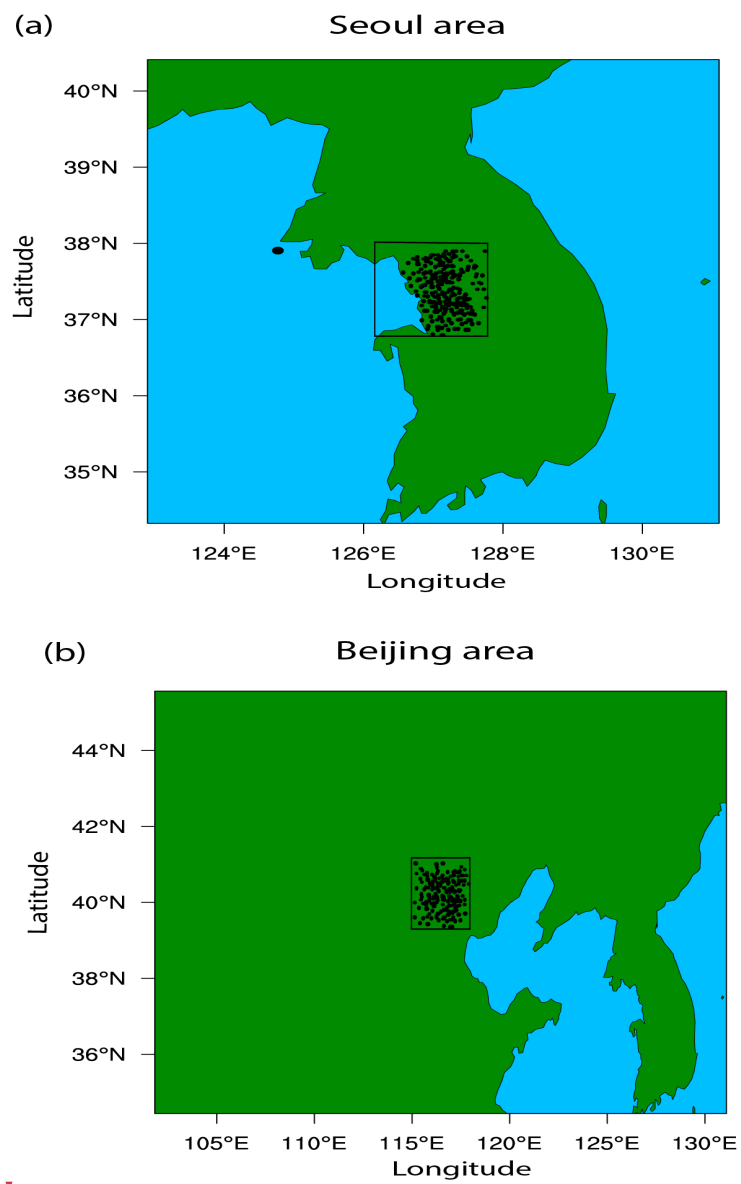
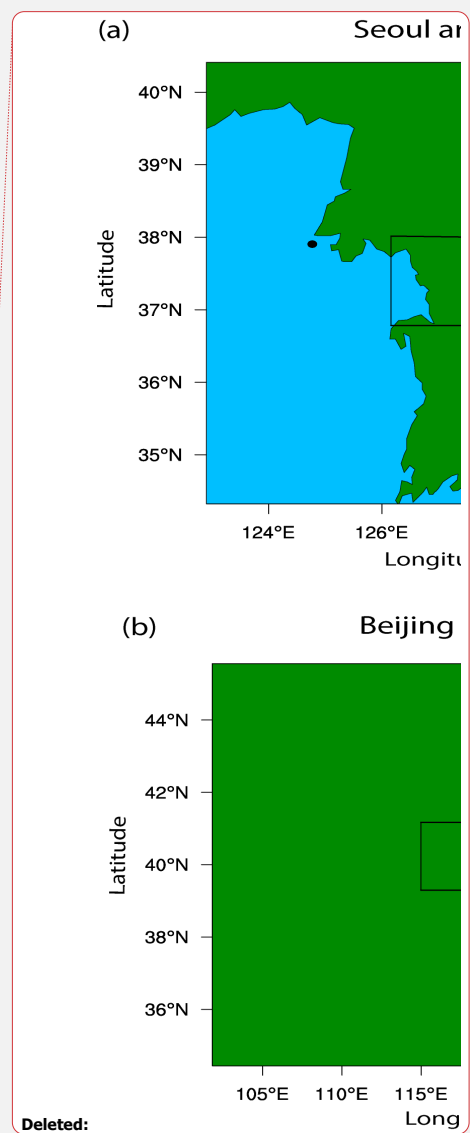
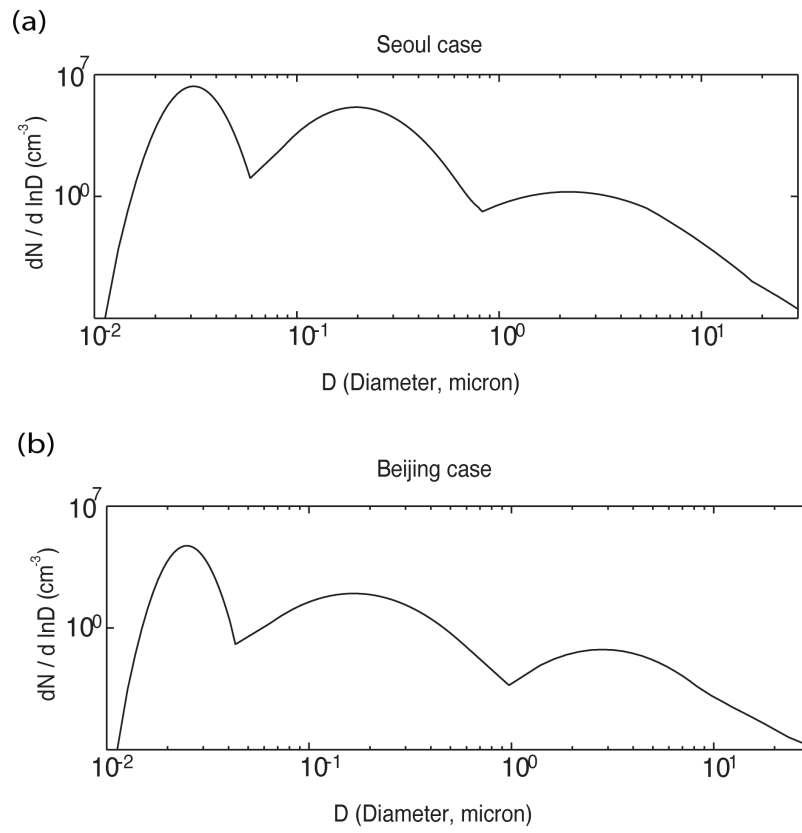
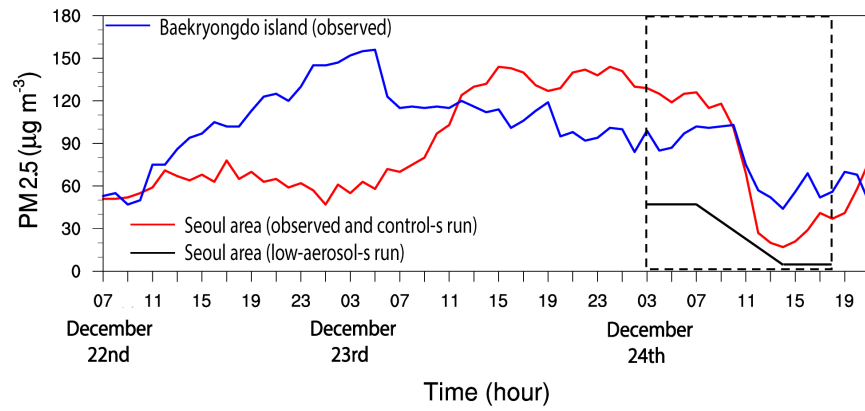


Figure 2

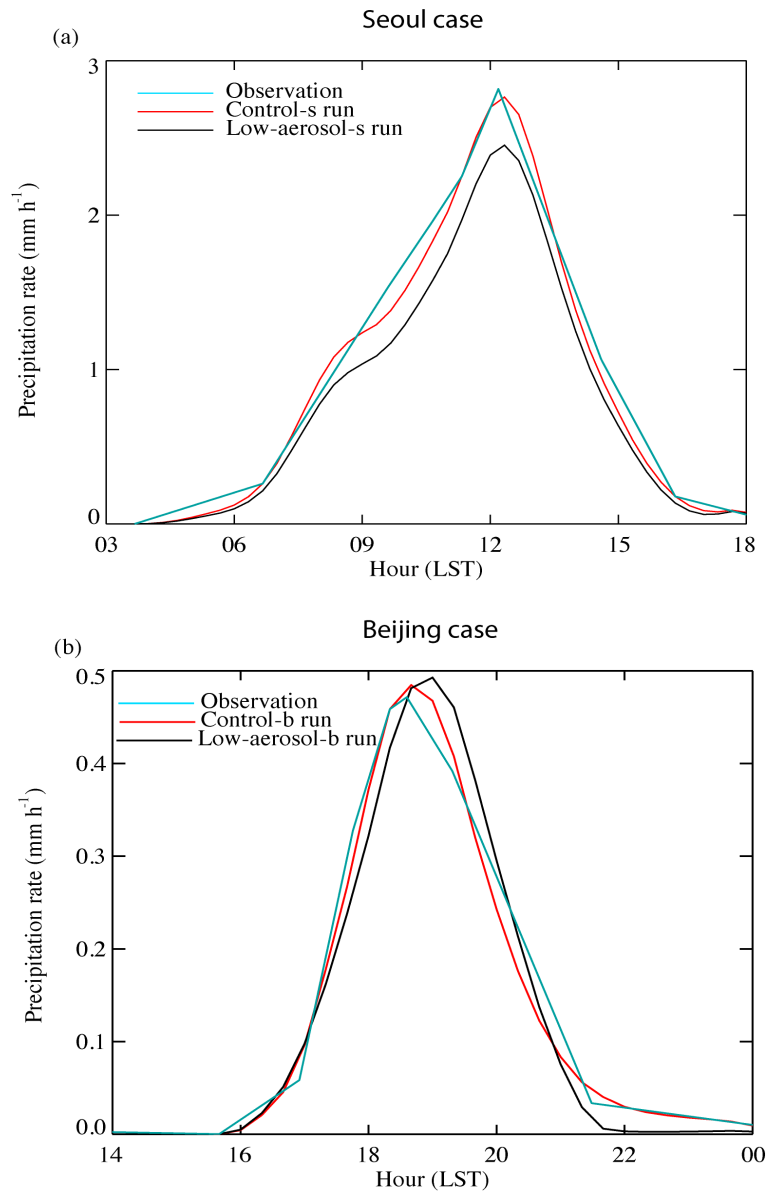


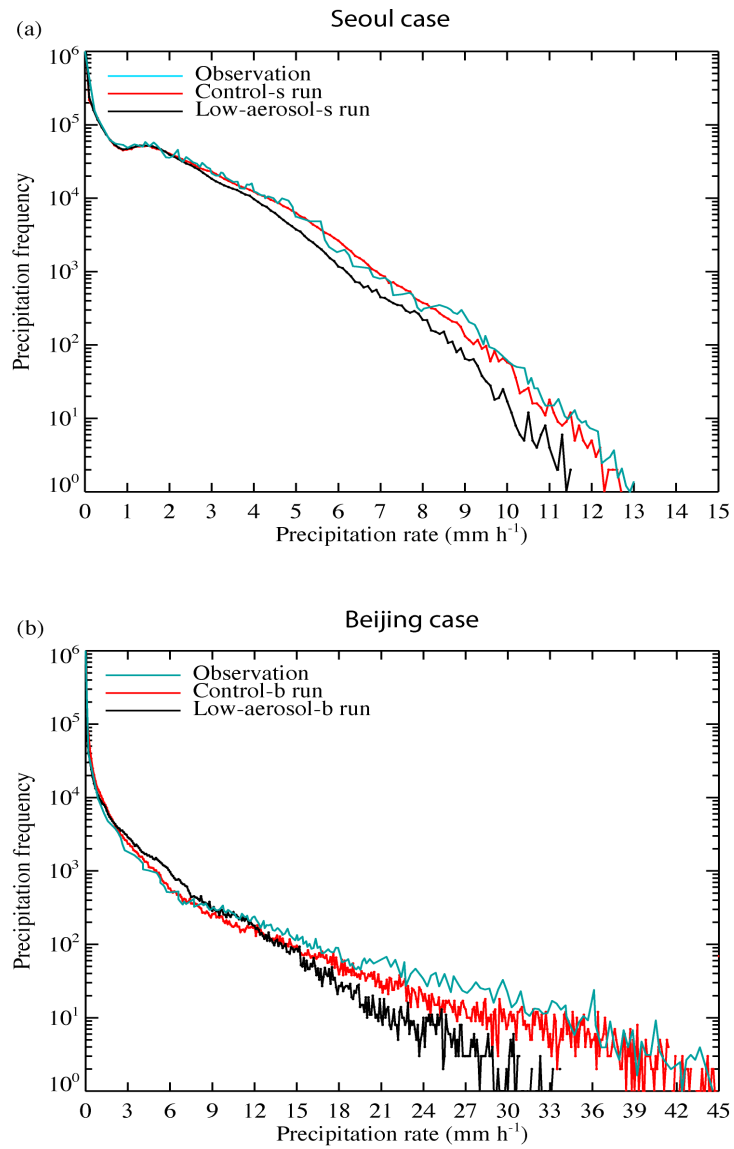


**Figure 3**



**Figure 4**

**Figure 5**

**Figure 6**

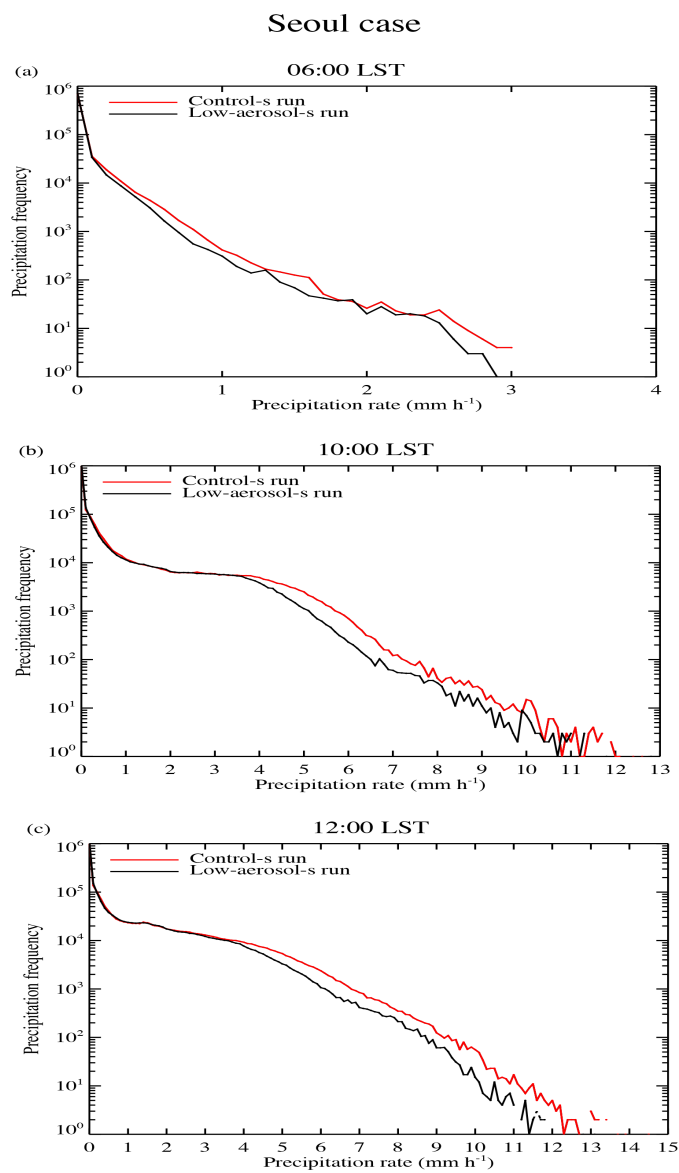
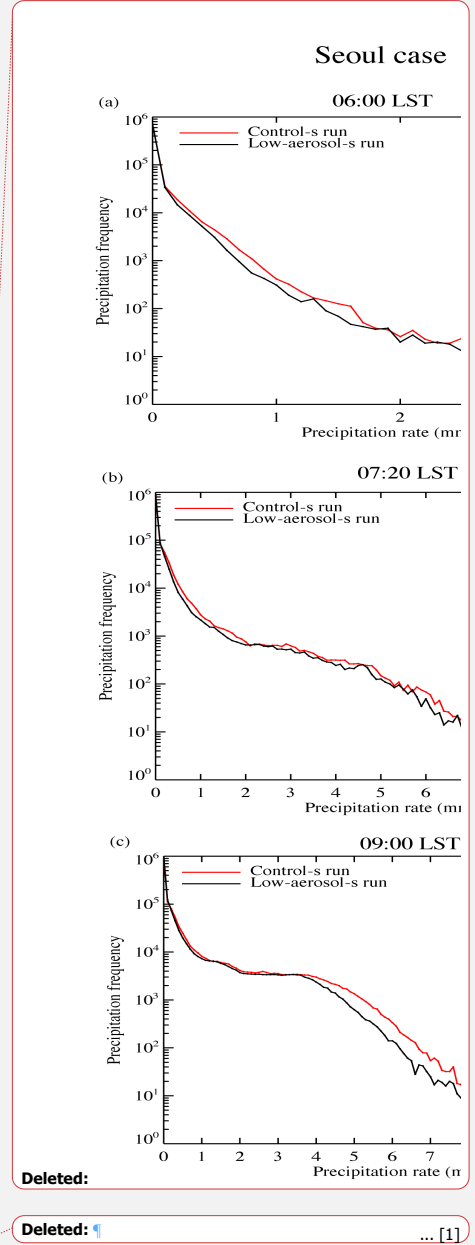
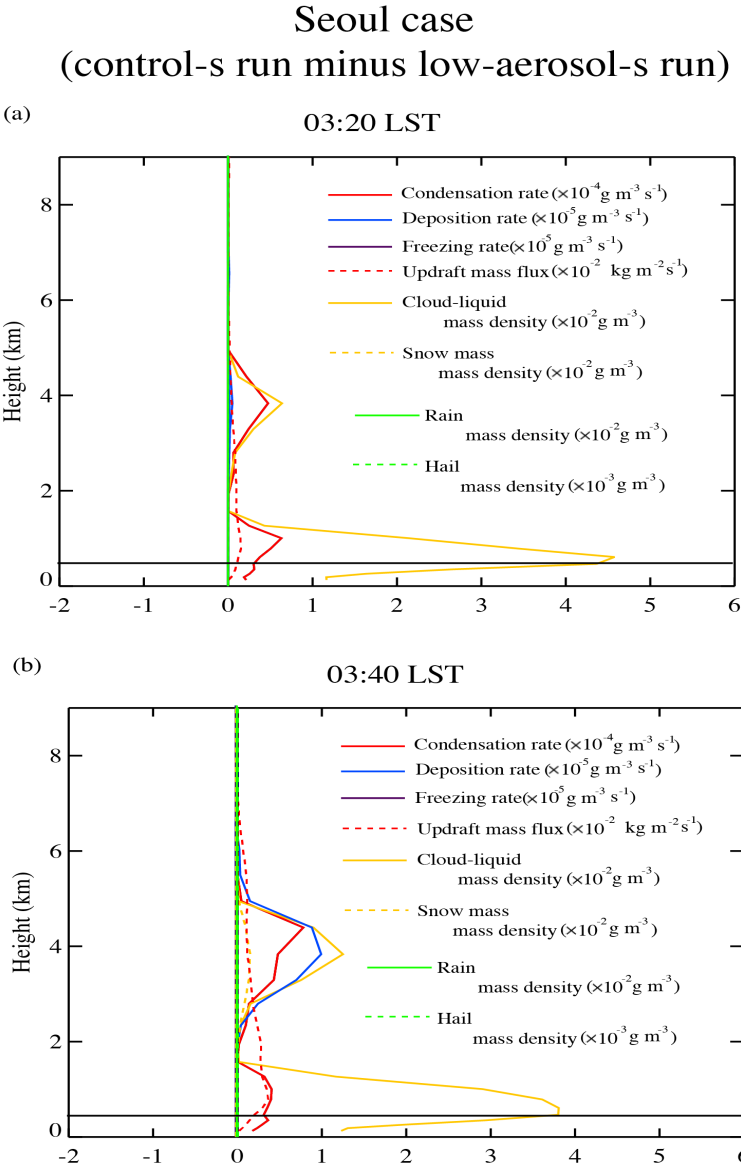


**Figure 7**

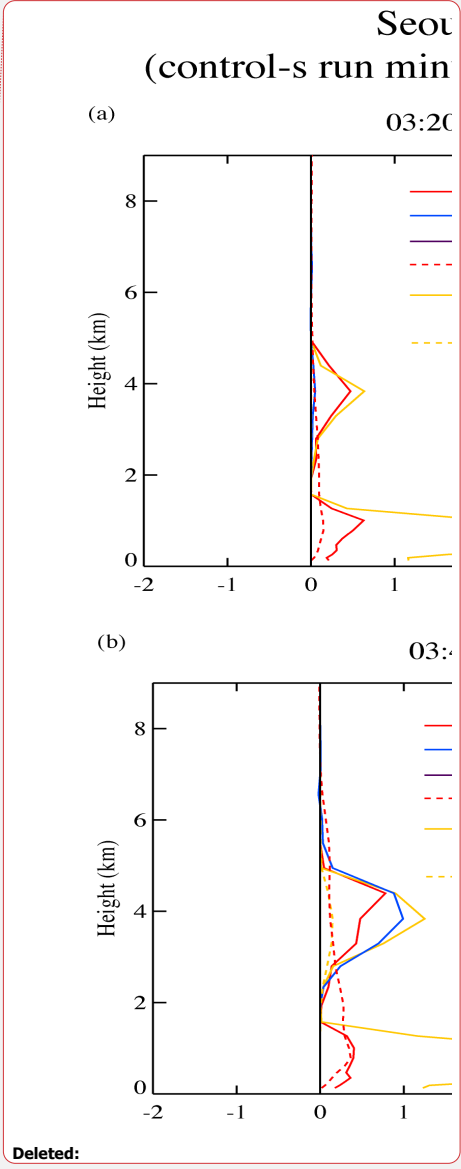


Deleted:

Deleted: [1]



**Figure 8**



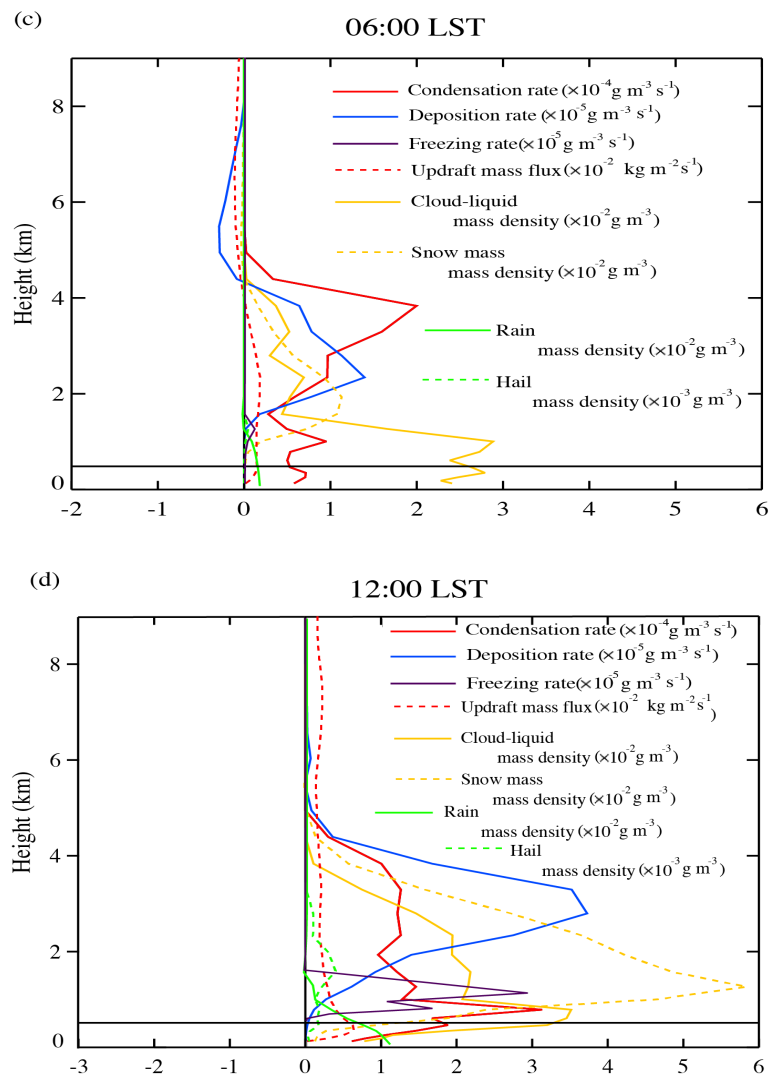
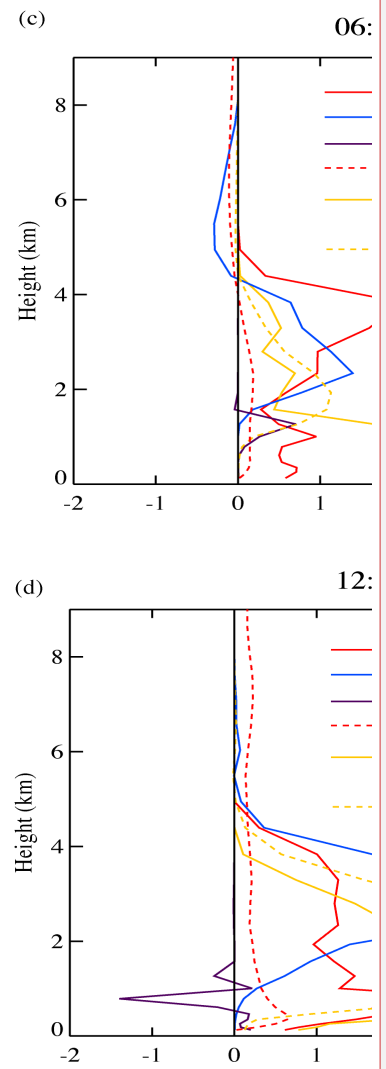


Figure 8



Deleted:

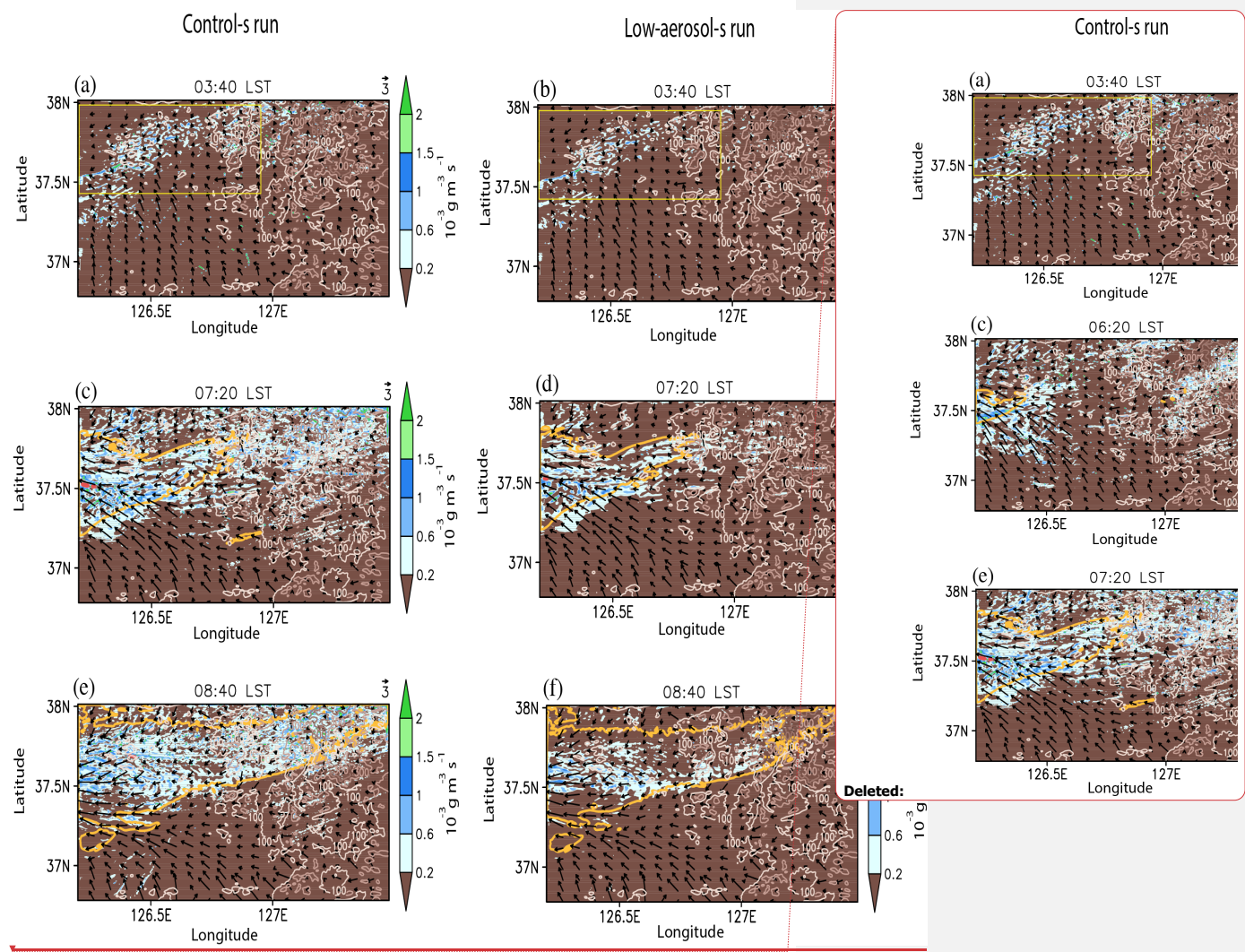


Figure 9

Deleted:



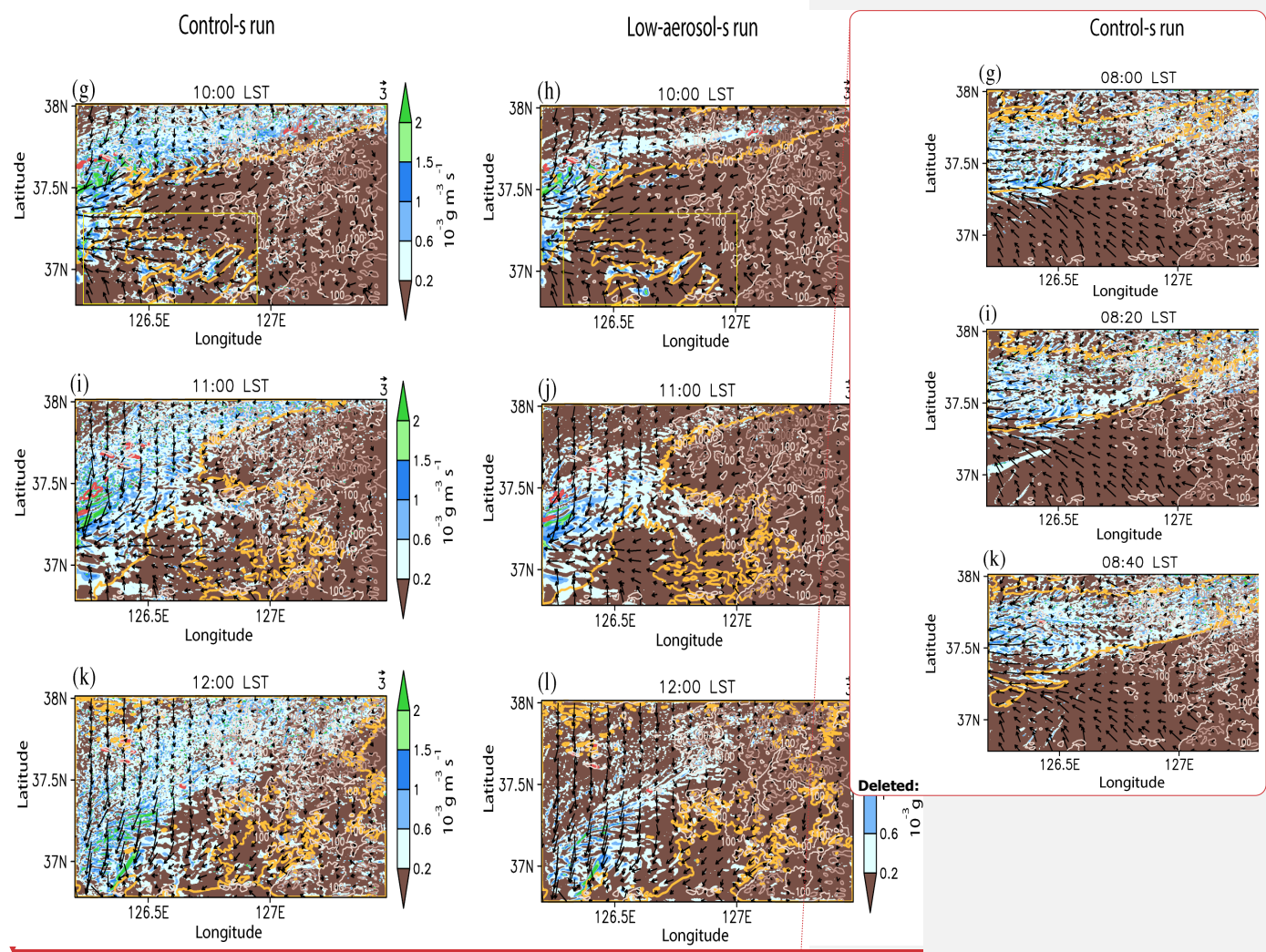
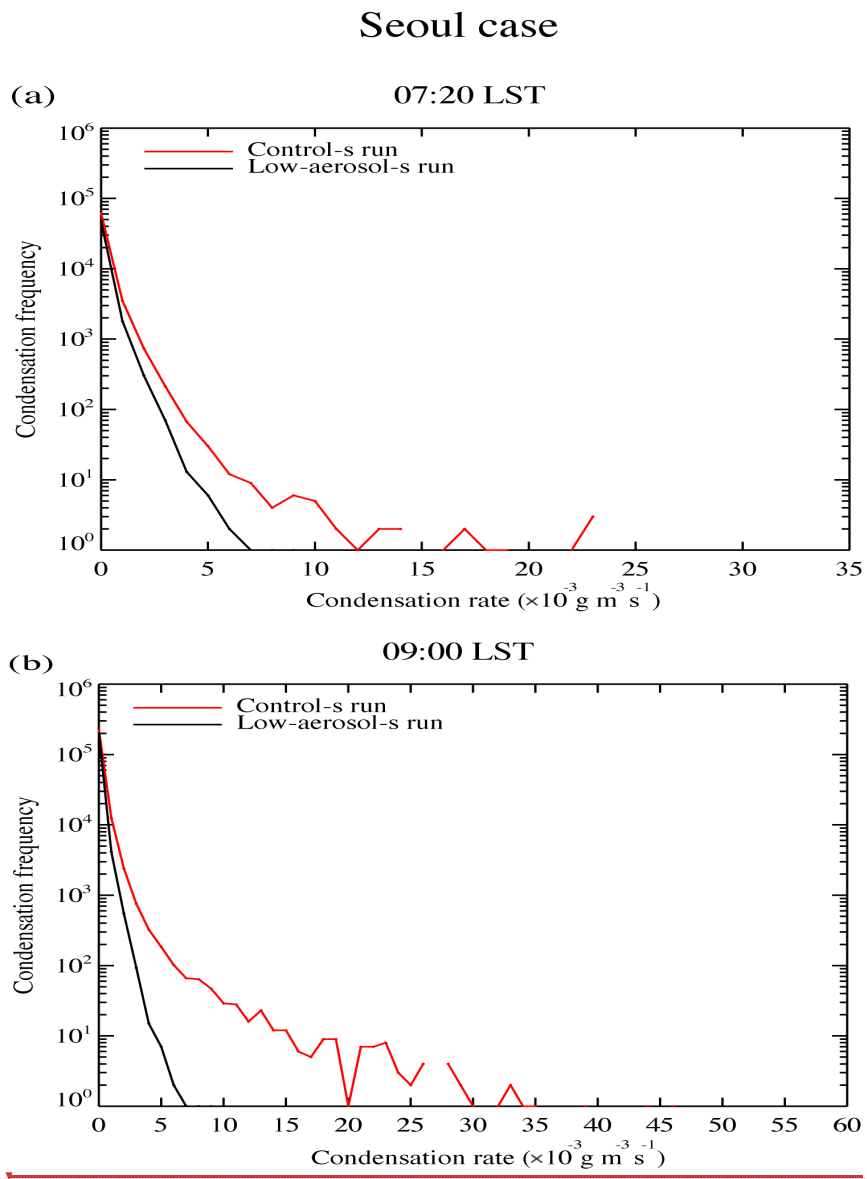
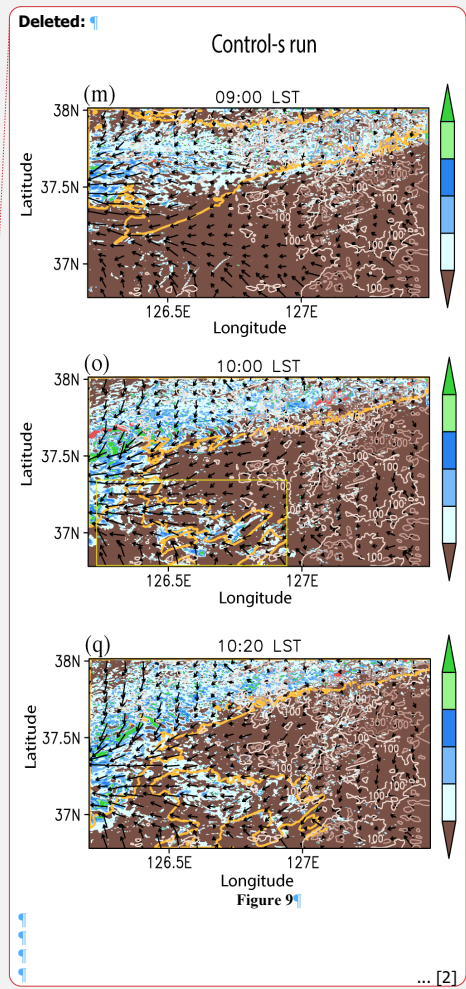
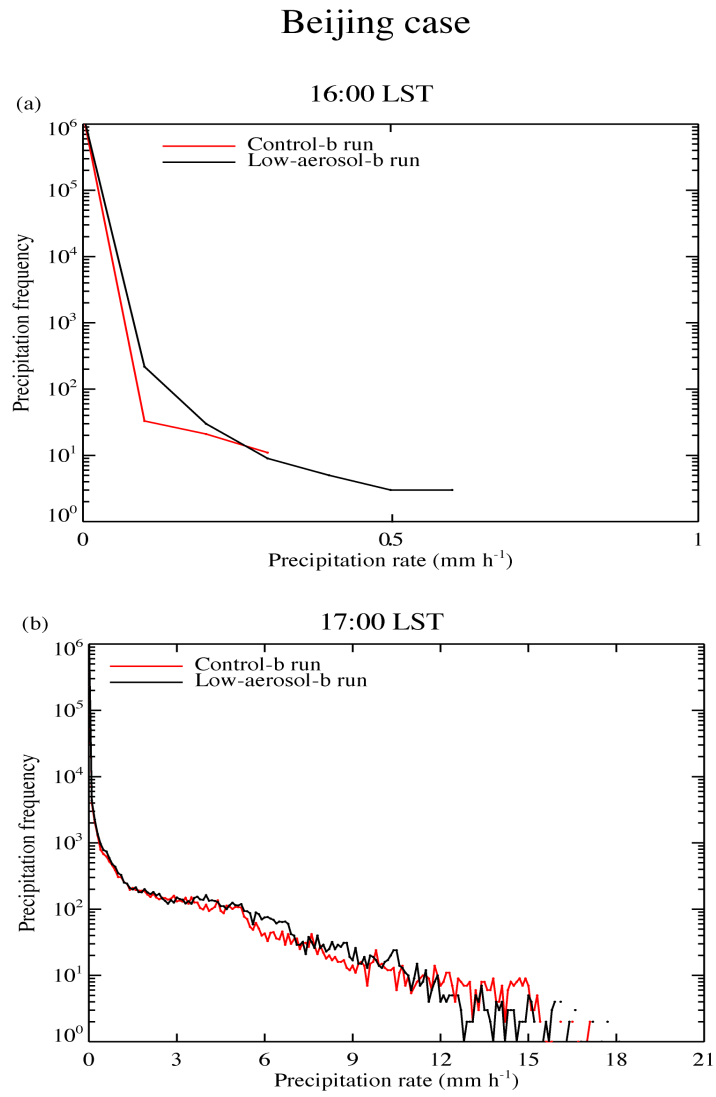


Figure 9

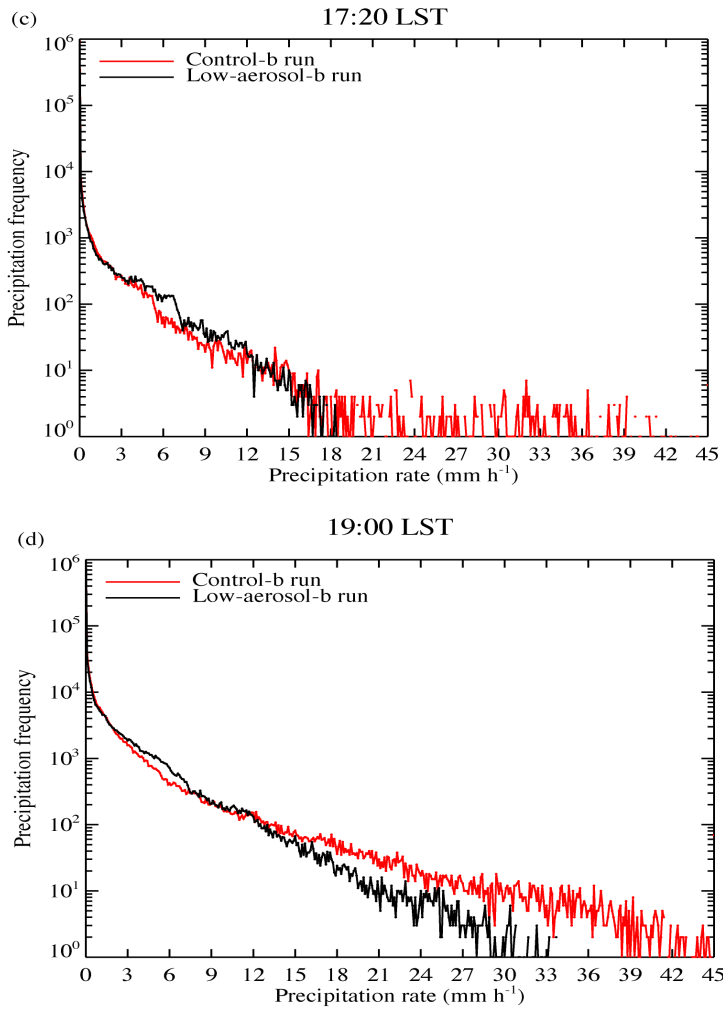


**Figure 10**

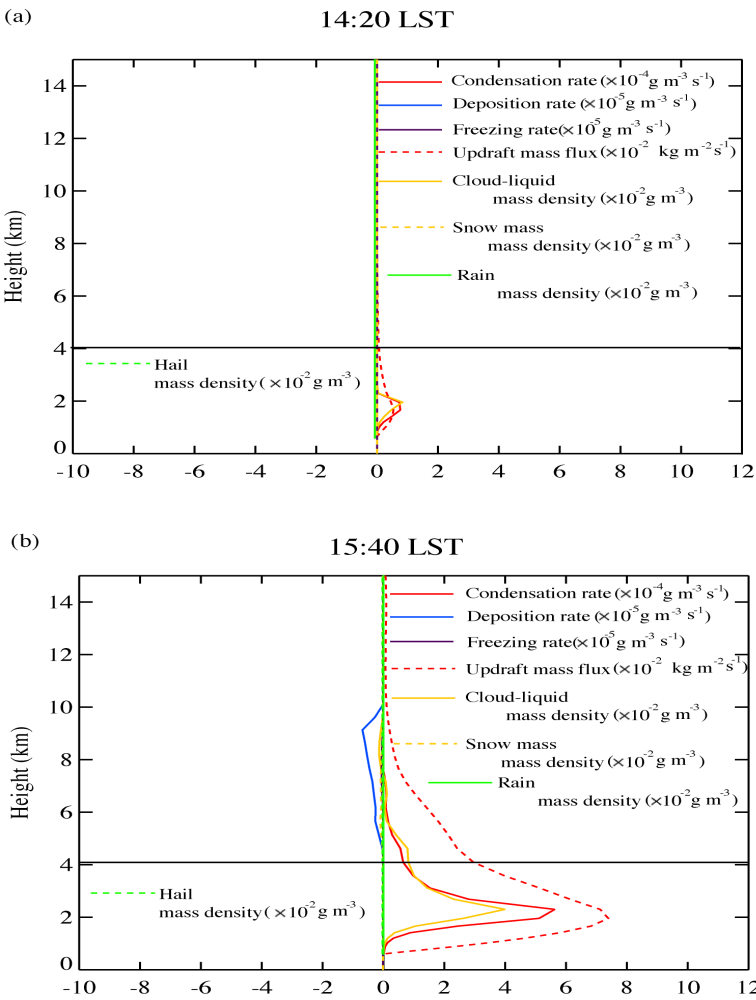




**Figure 11**

**Figure 11**

Beijing case  
(control-b run minus low-aerosol-b run)



Beiji  
(control-b run mir

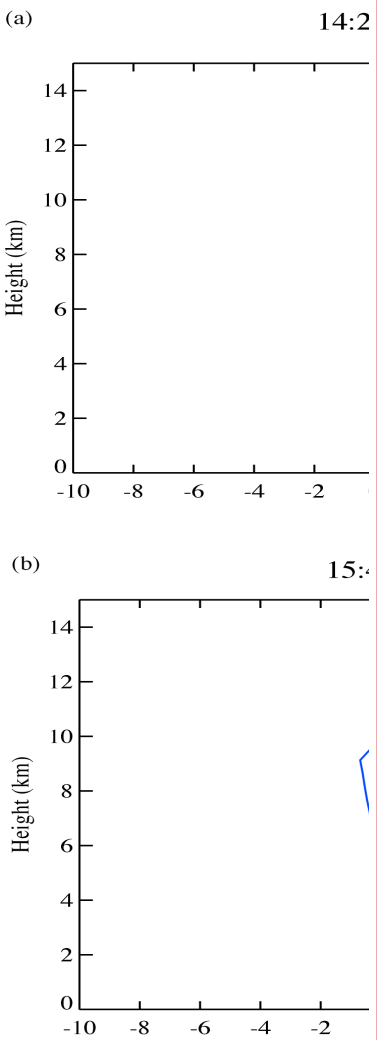


Figure 12

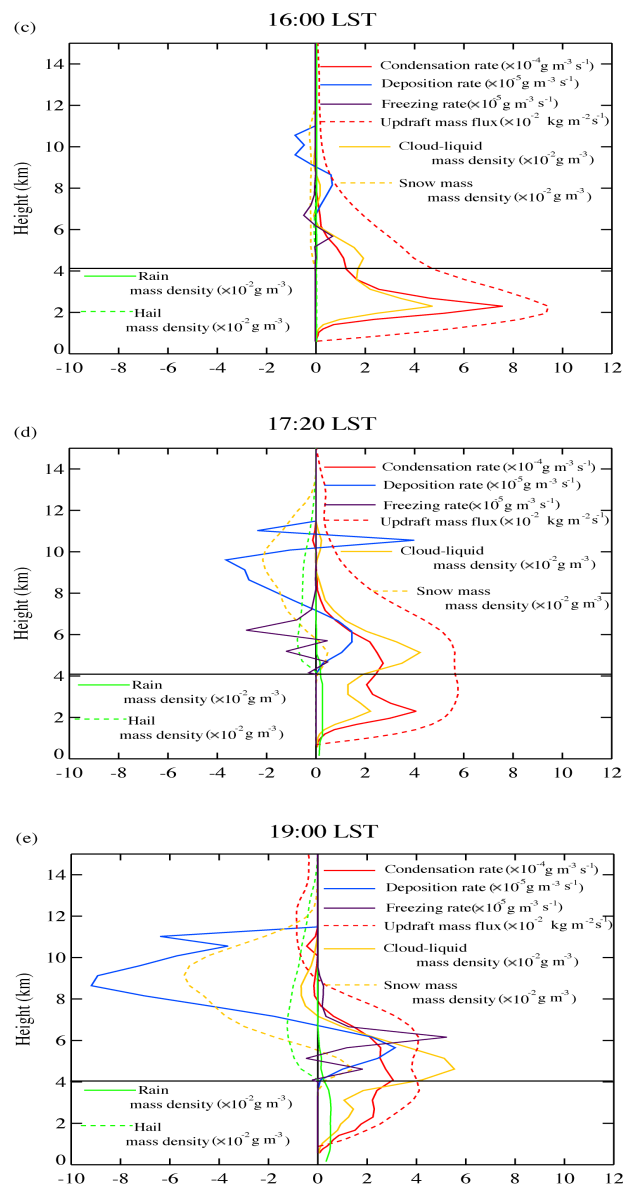
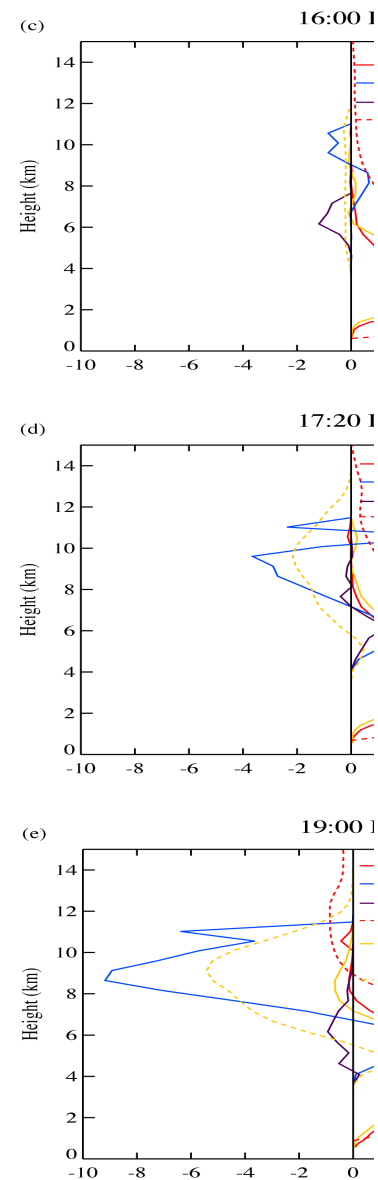
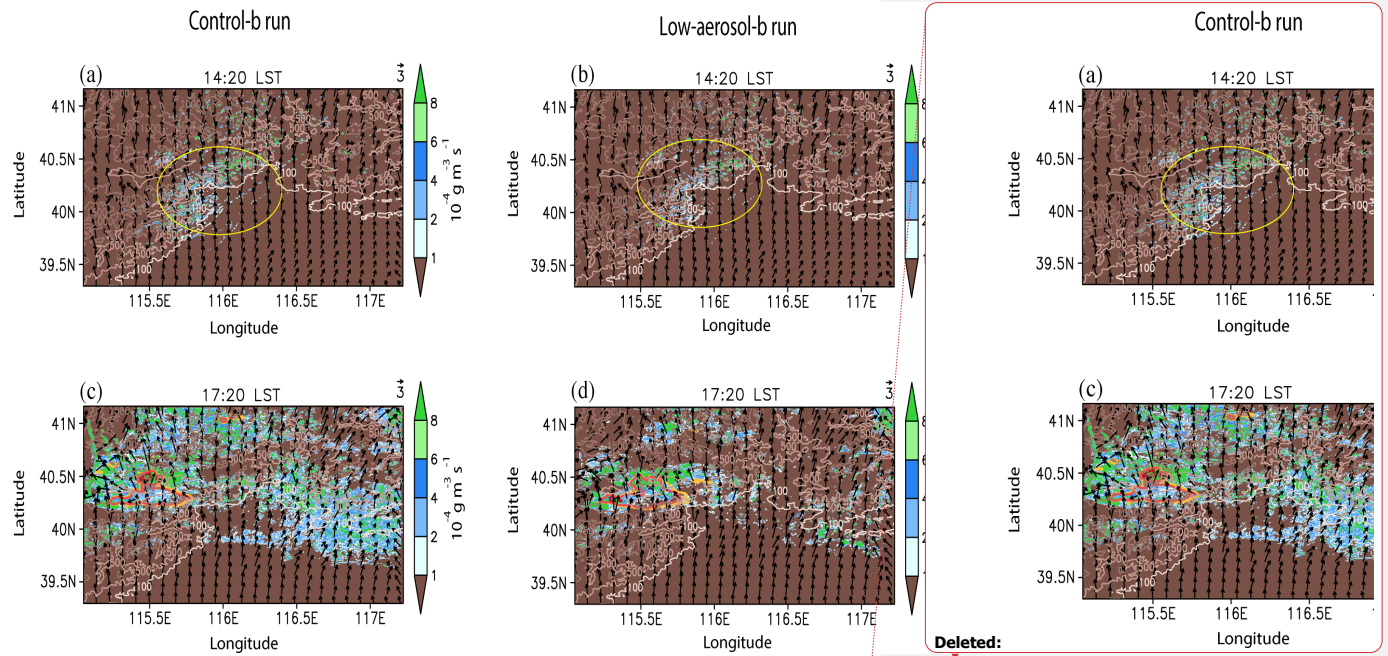


Figure 12



Deleted:  
Deleted:



**Figure 13**

Deleted:

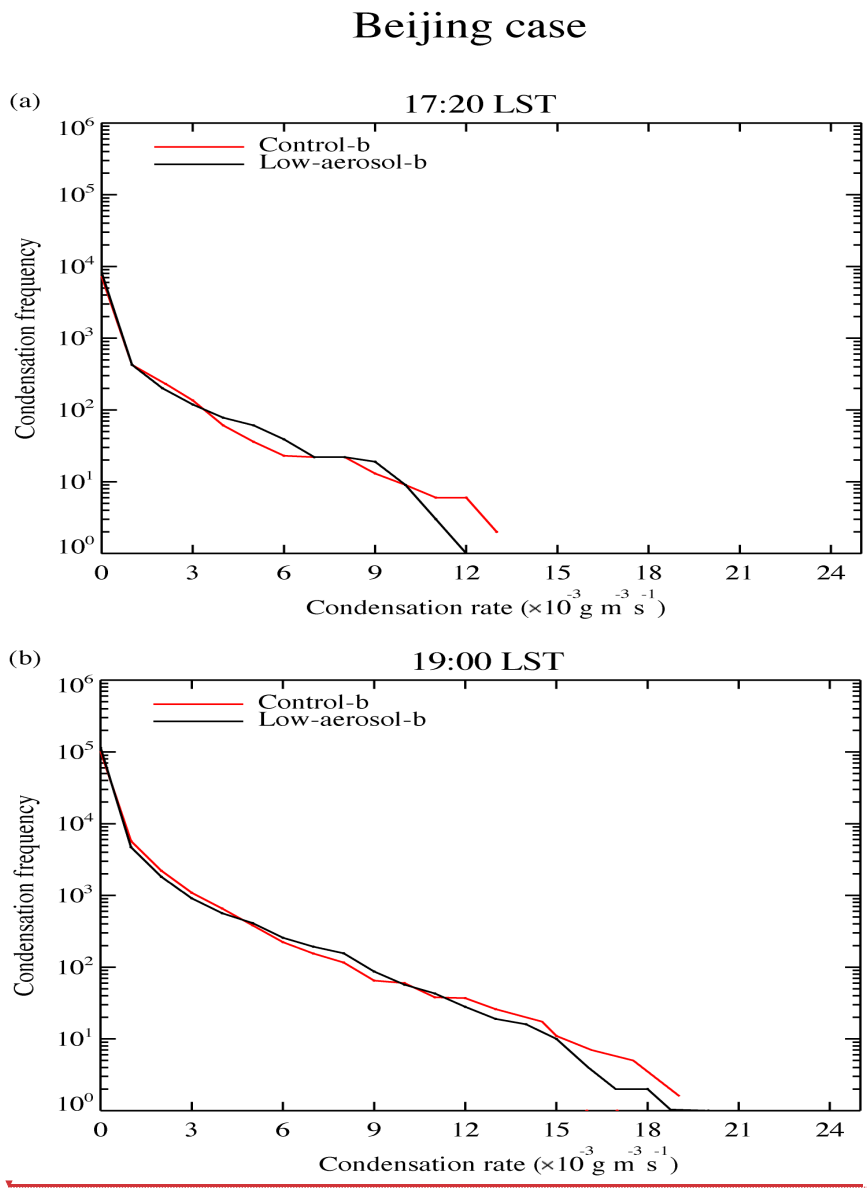


**Figure 14**

**Beiji**

(a) 17:

(b) 19:

**Deleted:**

**Formatted:** Line spacing: single, Tab stops: Not at 1.28"

**Deleted:**

**Deleted:**



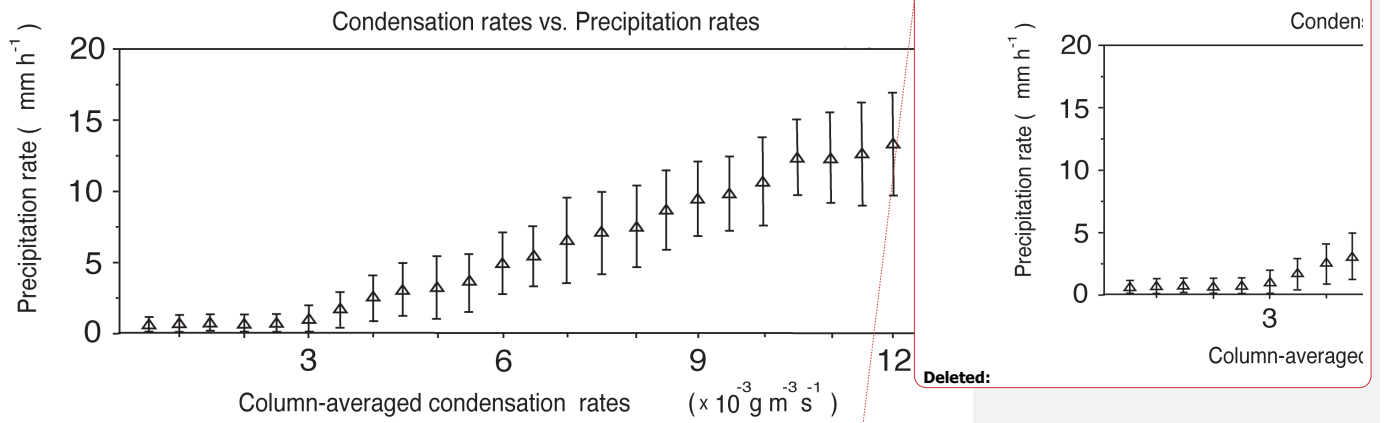


**Figure 15**

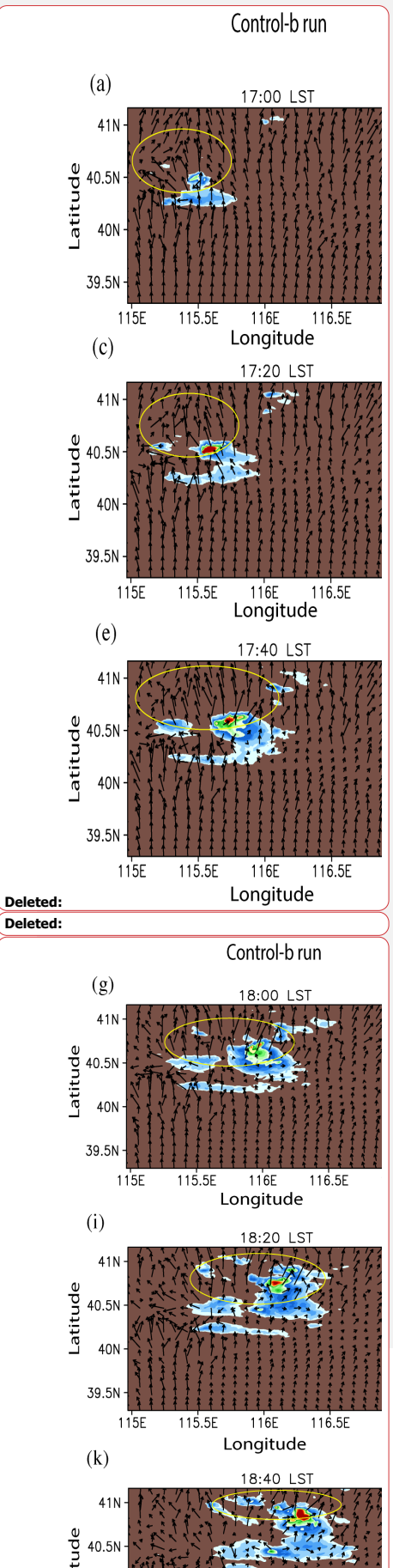


**Figure 16**

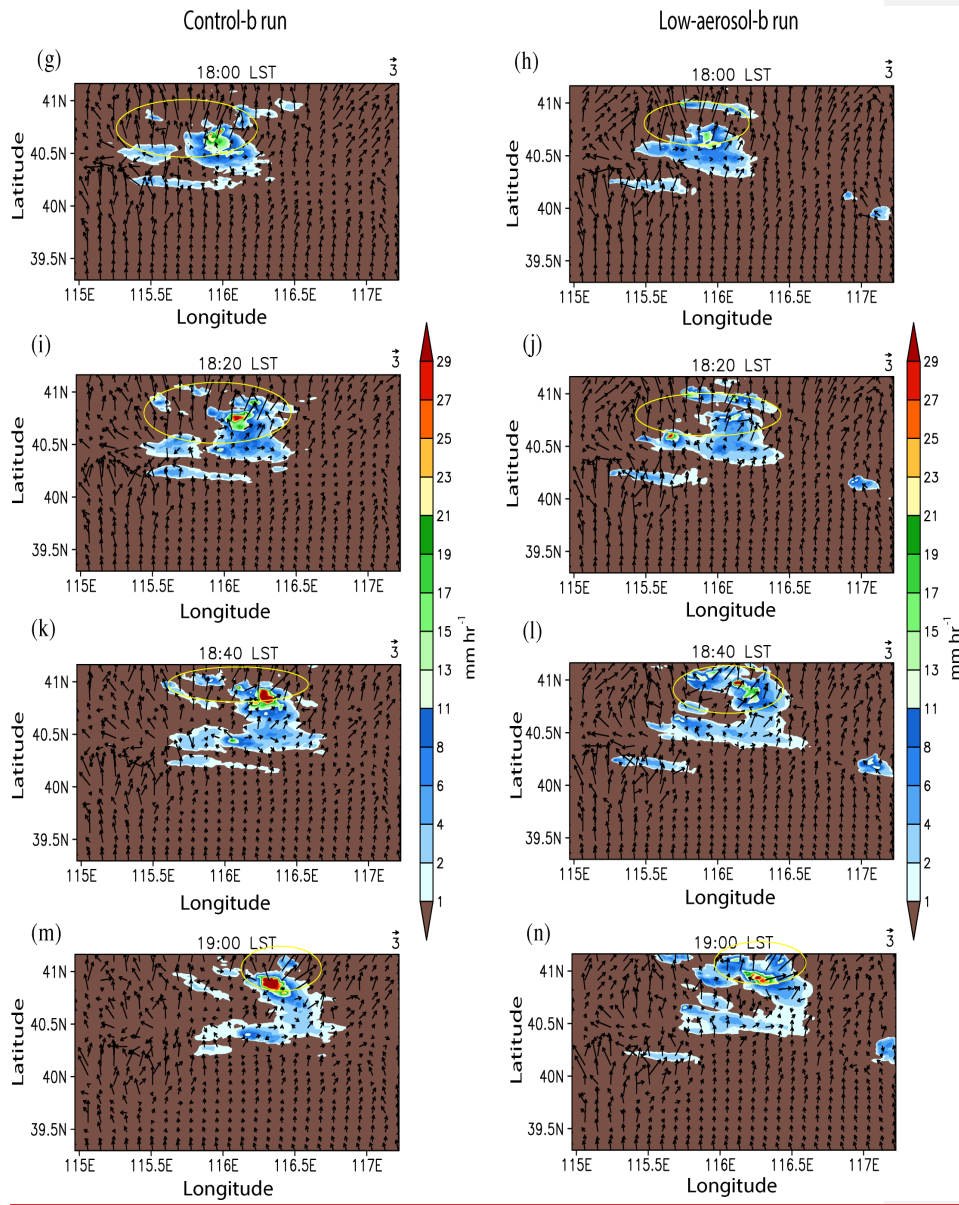


Figure 16

Deleted:

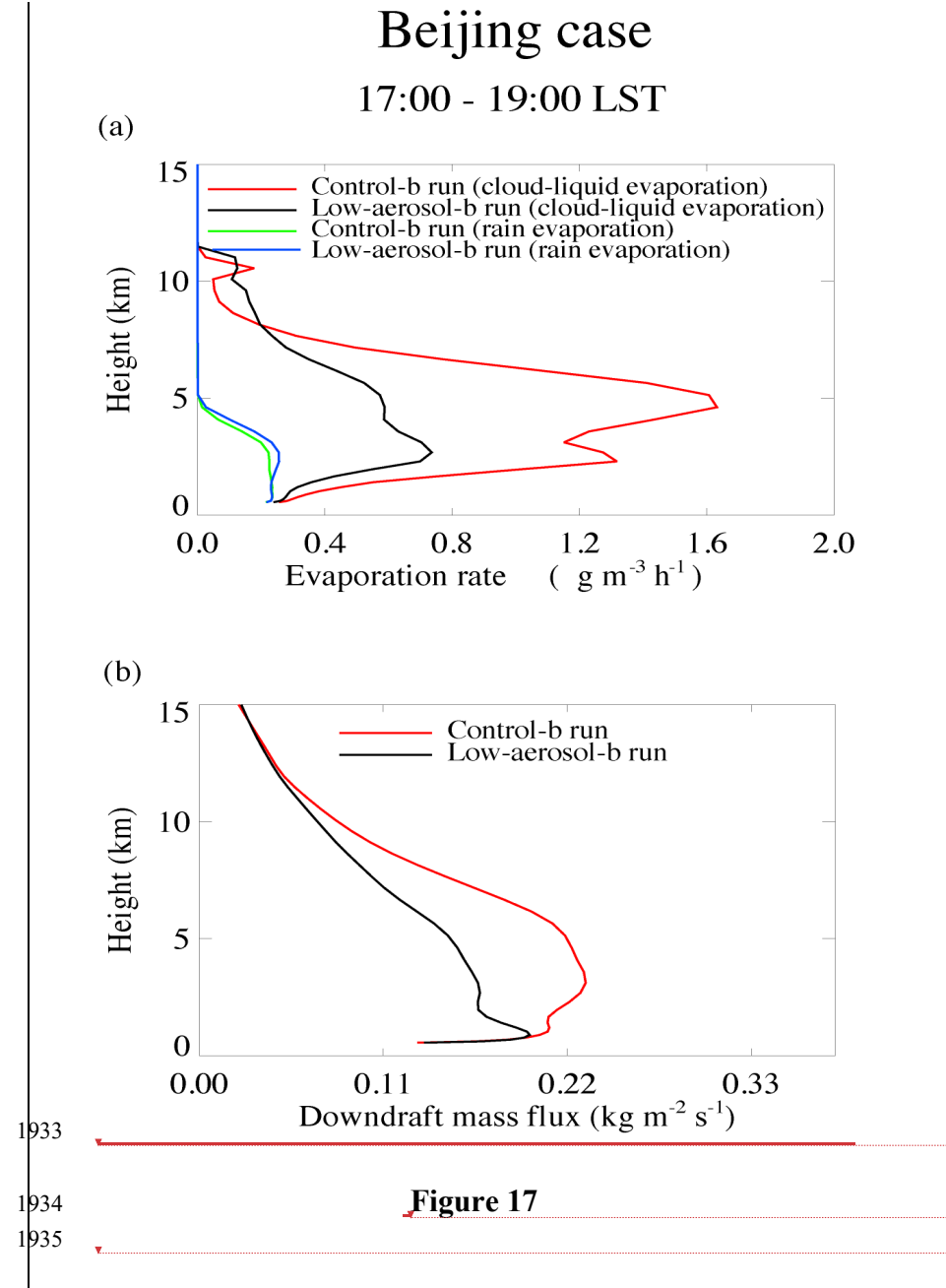
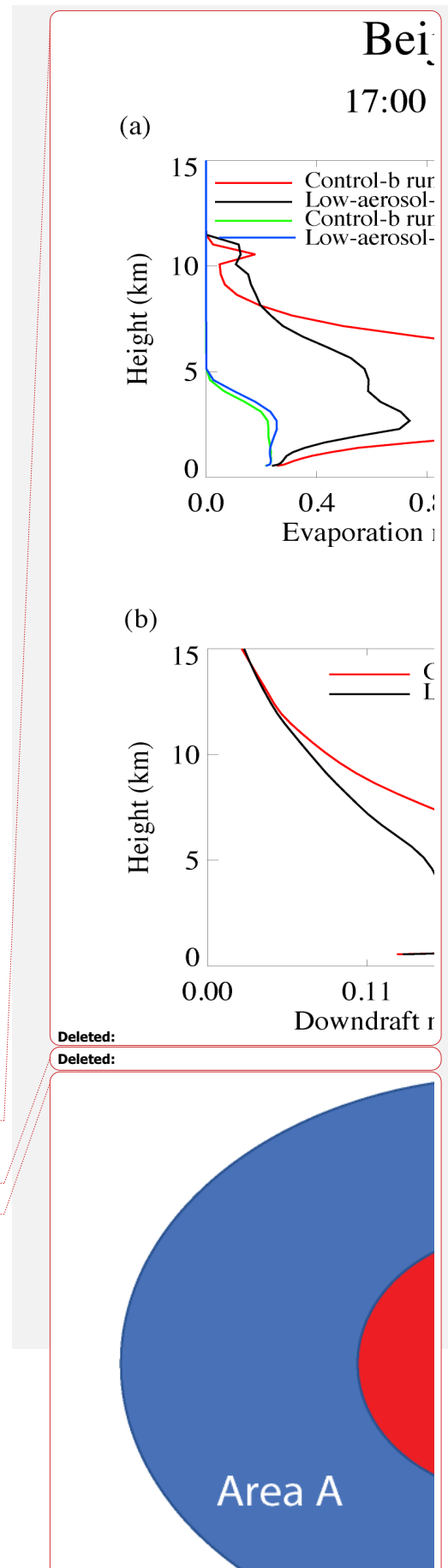


Figure 17



Page 49: [1] Deleted	Seoung Soo Lee	2/13/22 7:02:00 AM
----------------------	----------------	--------------------

Page 54: [2] Deleted	Seoung Soo Lee	2/13/22 8:31:00 AM
----------------------	----------------	--------------------

Page 64: [3] Deleted	Seoung Soo Lee	2/19/22 9:04:00 AM
----------------------	----------------	--------------------